

The Impact of the New ⁵⁹Fe Decay Rates on ⁶⁰Fe and ²⁶Al Nucleosynthesis in Massive Stars.

BINGYANG TAN,^{1,2} WENYU XIN,³ RUIZHENG JIANG,^{1,2} GANG ZHAO,^{1,2} AND KOH TAKAHASHI⁴

¹CAS Key Laboratory of Optical Astronomy, National Astronomical Observatories, Chinese Academy of Sciences, Beijing 100101, People's Republic of China

²School of Astronomy and Space Science, University of Chinese Academy of Sciences, Beijing 100049, People's Republic of China

³Institute of Astronomy and Physics, Inner Mongolia University, Hohhot 010021, People's Republic of China

⁴National Astronomical Observatory of Japan, National Institutes for Natural Science, 2-21-1 Osawa, Mitaka, Tokyo 181-8588, Japan

ABSTRACT

The diffuse γ -ray emission from short-lived radioactive ²⁶Al and ⁶⁰Fe provides a direct probe of ongoing nucleosynthesis in the Galaxy. However, theoretical models have long struggled to reproduce the observed ⁶⁰Fe/²⁶Al flux ratio, typically predicting values significantly higher than constraints derived from INTEGRAL/SPI observations. In this work, we investigate the impact of the recently measured, temperature-dependent stellar β^- decay rate of ⁵⁹Fe on the nucleosynthesis of these isotopes. We compute a grid of non-rotating massive star models (14–80 M_{\odot}) at solar metallicity using the MESA code, coupled with a rigorous numerical resolution analysis. We find that the updated rate significantly suppresses the net production of ⁶⁰Fe by approximately 0.28 dex ($\sim 47\%$) compared to models using LMP theoretical rates, while leaving ²⁶Al yields virtually unchanged. This reduction is primarily driven by the enhanced β^- decay during convective carbon shell burning. Integrating these yields over a standard Salpeter Initial Mass Function, we predict a Galactic flux ratio of ~ 0.18 , which is in excellent agreement with the observed value of 0.184 ± 0.042 . Furthermore, this ratio exhibits a weak dependence on the IMF slope. Our results indicate that the updated nuclear physics input significantly alleviates the long-standing ⁶⁰Fe overproduction problem, bringing theoretical predictions into much closer alignment with current Galactic observations.

Keywords: Nuclear astrophysics (1129) — Massive stars (732) — Stellar nucleosynthesis (1616) — Core-collapse supernovae (304) — γ -ray astronomy (628)

1. INTRODUCTION

Observations of diffuse γ -ray lines emitted from the decay of radioactive isotopes ²⁶Al (at 1.809 MeV) and ⁶⁰Fe (at 1.173 and 1.332 MeV) provide a direct probe of ongoing nucleosynthesis in the Milky Way (Mahoney et al. 1982; Smith 2004; Wang et al. 2007, 2020; Diehl et al. 2021). With respective half-lives of 0.717 Myr for ²⁶Al (Coc et al. 1999; Banerjee et al. 2018) and 2.62 Myr for ⁶⁰Fe (Rugel et al. 2009; Wallner et al. 2015; Ostdiek et al. 2017), these isotopes trace nucleosynthetic events occurring within the last few million years.

All-sky map of the 1.809 MeV γ -ray emission suggests that massive stars and their subsequent core-collapse supernovae (CCSNe) are the primary production sites for ²⁶Al (Diehl et al. 1995; Prantzos 2004). As summarized by Diehl et al. (2021), while both isotopes ²⁶Al and ⁶⁰Fe

are synthesized in Asymptotic Giant Branch (AGB) and massive stars, the contribution from AGB stars is generally considered minor and remains subject to significant uncertainties inherent in current stellar models, especially for ⁶⁰Fe. In the context of massive stars, given that both isotopes share similar astrophysical origins and comparable half-lives, the ⁶⁰Fe/²⁶Al γ -ray flux ratio is expected to be largely insensitive to the details of their Galactic distribution. Under the assumption of a steady-state equilibrium, where the continuous production of these isotopes is balanced by their radioactive decay, the observed ratio could be directly compared to the nucleosynthesis yields from massive star models by converting the mass yields with a factor of 26/60. Austin et al. (2017) considered the ⁶⁰Fe/²⁶Al yield ratio as a ‘robust observable’ for massive star models. However, systematic discrepancies remain between theoretical predictions and the flux ratios observed by Spectrometer on the International Gamma Ray Astrophysics Laboratory (INTEGRAL/SPI, Vedrenne et al. 2003),

and Reuven Ramaty High-Energy Solar Spectroscopic Imager (RHESSI, [Lin et al. 2002](#)).

The first observational constraint on Galactic ^{60}Fe emission was derived from RHESSI data ([Smith 2004](#)), yielding an $^{60}\text{Fe}/^{26}\text{Al}$ flux ratio of approximately 0.4. Subsequent observations by INTEGRAL/SPI have refined this value, with reported flux ratios ranging from 0.08 to 0.22, adapting different analysis methods ([Wang et al. 2007](#); [Bouchet et al. 2011, 2015](#)). The most recent results from 15 years of SPI data is presented by [Wang et al. \(2020\)](#). The $^{60}\text{Fe}/^{26}\text{Al}$ flux ratio of $(18.4 \pm 4.2)\%$ is determined using a specific parameterized spatial morphology model (e.g., an exponential disk). However, because the spatial distribution of ^{60}Fe is not yet as well-constrained as that of ^{26}Al , a broader range of 0.2–0.4 is estimated by taking into account the sensitivity of the results to different spatial tracer templates. This broader range reflects the systematic uncertainties inherent in deconvolving diffuse emission from the Galactic plane. This observational range is consistent with the lower limit of 0.1 inferred from deep-sea sediments data ([Feige et al. 2018](#)). Notably, early predictions by [Timmes et al. \(1995\)](#) (~ 0.16) align well with these subsequent observations. However, a persistent discrepancy has emerged in later theoretical studies, with contemporary models systematically overproducing ^{60}Fe relative to ^{26}Al . Specifically, several widely used models predict flux ratios that exceed observed values by a factor of 3 to 10 ([Woosley & Heger 2007](#); [Sukhbold et al. 2016](#); [Austin et al. 2017](#)). In contrast, certain studies ([Limongi & Chieffi 2006](#); [Chieffi & Limongi 2013](#)) yield more consistent results in the range of 0.1 to 0.3, which align more closely with the observational constraints. Such a tension suggests that our understanding of the nucleosynthesis of these two isotopes in massive stars is unsettled, and the general overproduction of ^{60}Fe remains a fundamental challenge in theoretical predictions.

The predicted yields of ^{26}Al and ^{60}Fe are known to be sensitive to several key stellar modeling uncertainties. In particular, the inclusion of stellar rotation can fundamentally alter the nucleosynthetic output by inducing internal mixing and enhancing mass-loss rates. For ^{26}Al , the contribution from stellar winds is critically dependent on these processes, as rotationally induced mixing can dredge up synthesized material to the stellar surface, where it is subsequently ejected before the supernova stage. Previous studies have extensively explored how different treatments of rotation and mass-loss prescriptions impact the resulting ^{60}Fe and ^{26}Al yields ([Ekström et al. 2012](#); [Limongi & Chieffi 2018](#); [Brinkman et al. 2021](#); [Falla et al. 2025](#)). While adjustments to these modeling parameters can sometimes improve the agree-

ment with Galactic observations, they often introduce further complexities and degeneracies within the stellar evolutionary tracks.

However, a more fundamental and perhaps critical source of this discrepancy may lie in the nuclear physics inputs, as [Woosley & Heger \(2007\)](#) suggested, the unmeasured cross sections governing the production of ^{60}Fe could be a significant source of uncertainty, for instance, the β^- decay rate of ^{59}Fe . In the C and Ne burning shells of massive stars where ^{60}Fe is primarily synthesized, ^{59}Fe acts as a pivotal branching point in s-process pathways. The competition between neutron capture on ^{59}Fe to form ^{60}Fe and its β^- decay back to ^{59}Co directly influences the final yields of ^{60}Fe . For decades, stellar models have relied on theoretical rates from [Langanke & Martínez-Pinedo \(2001\)](#) (hereafter LMP), which were based on large-scale shell-model calculations.

In recent years, a breakthrough experiment by [Gao et al. \(2021\)](#) provided the first experimental constraints on the key β^- decay transitions of ^{59}Fe . Their results indicate that at temperatures relevant to C and Ne shell burning ($T \gtrsim 1$ GK), the stellar decay rate is nearly three times higher than the LMP prediction, directly suppressing ^{60}Fe production. Indeed, [Gao et al. \(2021\)](#) also performed a stellar model test for an $18 M_{\odot}$ star, finding that the new rate reduces the ^{60}Fe yield by 40% compared to the LMP rate. To fully evaluate the impact on the Galactic $^{60}\text{Fe}/^{26}\text{Al}$ flux ratio, however, a more extensive grid of massive star models across a wide mass range is essential to isolate the impact of this decay uncertainty on the final yields.

Regarding the aforementioned branching-point competition, a recent measurement by [Spyrou et al. \(2024\)](#) reported an enhancement by a factor of 1.6 to 2.1 in the ^{59}Fe neutron capture rate, which would conversely promote ^{60}Fe production. While such updates should ideally be integrated into stellar models concurrently, implementing multiple significant adjustments simultaneously makes it difficult to disentangle the individual nucleosynthetic impact of each physical change. Therefore, in this work, to facilitate a clear comparison with previous theoretical studies, we retain the standard LMP rate for the neutron capture channel. This strategy allows us to focus exclusively on the consequences of the enhanced β^- decay rate, which itself represents a substantial threefold revision and a key mechanism for alleviating the ^{60}Fe overproduction problem.

In this paper, we systematically investigate the impact of this updated ^{59}Fe decay rate on the nucleosynthesis of ^{60}Fe in massive stars and the resulting Galactic $^{60}\text{Fe}/^{26}\text{Al}$ flux ratio. Utilizing the Modules for Experiments in Stellar Astrophysics (MESA, version 12115;

Paxton et al. 2011, 2013, 2015, 2018; Jermyn et al. 2023), we computed a comprehensive grid of stellar models with initial masses from 14 to $80 M_{\odot}$ at solar metallicity. We compare two distinct sets of models: the "DR" series using default LMP rates and the "NR" series incorporating the new experimental rate from Gao et al. (2021). By integrating these yields over a standard Initial Mass Function (IMF), we quantify how the new nuclear data reconciles theoretical predictions with the latest INTEGRAL observations.

This paper is organized as follows. Section 2 details our numerical framework, including the pre-supernova stellar models, the treatment of core-collapse explosions, and the integration procedure used to calculate the Galactic $^{60}\text{Fe}/^{26}\text{Al}$ flux ratio. In Section 3, we present the basic evolutionary properties of our models and analyze the primary nucleosynthesis yields, specifically highlighting the physical mechanism of ^{60}Fe suppression via a representative $30 M_{\odot}$ case study. Section 4 examines the broader implications of these results, addressing the mass-dependent role of fallback, comparisons with current INTEGRAL observations, and the impact of systematic uncertainties. Finally, our main conclusions are summarized in Section 5.

2. NUMERICAL METHODS

To quantify the impact of updated nuclear data on the Galactic $^{60}\text{Fe}/^{26}\text{Al}$ γ -ray flux ratio, we perform a multi-stage numerical investigation. Our methodology bridges microscopic nuclear reaction rates with macroscopic stellar populations through three steps: (1) the construction of robust pre-supernova (pre-SN) models incorporating a refined nuclear network; (2) the simulation of the core-collapse supernova (CCSN) explosion via a parameterized thermal bomb to account for explosive nucleosynthesis; and (3) the integration of these individual yields over the initial mass function (IMF). In the following subsections, we detail the input physics, the implementation of the new ^{59}Fe decay rate, and the resolution convergence tests that ensure the robustness of our nucleosynthetic yields. Finally, we describe our CCSN models and procedure for calculating the Galactic $^{60}\text{Fe}/^{26}\text{Al}$ γ -ray flux ratio from our model grid.

2.1. Pre-supernova Models

We employ the MESA stellar evolution code (version r121115) to simulate the evolution and nucleosynthesis of massive stars, from the zero-age main sequence (ZAMS) through the onset of core-collapse supernova (CCSN) phase. The pre-supernova models are evolved until any location within the iron core reaches an infall velocity of 1000 km s^{-1} . Our setup is based on

the `25M_pre_ms_to_core_collapse` test suite provided in the MESA distribution.

2.1.1. Basic Input Physics

We simulate a grid of massive star models with initial masses ranging from 14 to $80 M_{\odot}$. This range covers the primary contributors to the Galactic nucleosynthesis of ^{26}Al and ^{60}Fe (Limongi & Chieffi 2006; Woosley & Heger 2007; Diehl et al. 2021). Stars below $14 M_{\odot}$ are excluded as they yield significantly lower amounts of these isotopes. While stars exceeding $80 M_{\odot}$ could also contribute to the Galactic ^{26}Al budget through intense Wolf-Rayet (WR) wind activity (Palacios et al. 2005), we truncate our grid at this limit because such massive objects are prone to direct black hole formation, which potentially retains their nucleosynthetic products. The potential impact of this limited mass range on the integrated Galactic flux ratio is addressed in Section 4.3.3.

All models adopt an initial metallicity of $Z = 0.02$ with the solar abundance distribution from Grevesse & Sauval (1998). The initial helium mass fraction is set to $Y = 2Z + 0.24$ and the hydrogen mass fraction is $X = 1 - Y - Z$. For mass loss, the models are evolved with the Dutch prescriptions which includes de Jager et al. (1988) for cool stars, Vink et al. (2001) for hot hydrogen-rich stars, and Nugis & Lamers (2000) for Wolf-Rayet stars. We used a reduction factor of `Dutch_scaling_factor` = 0.8, consistent with Farmer et al. (2016) and Maeder & Meynet (2001).

Convective mixing is treated using the Ledoux criterion with a mixing length parameter $\alpha_{\text{mlt}} = 1.5$. We employ the diffusive exponential overshoot scheme (Herwig 2000) with MESA parameters $f = 0.01$ and $f_0 = 0.004$. These values, along with a semi-convection efficiency of $\alpha_{\text{semi}} = 0.01$, are chosen to ensure our stellar structures are consistent with established grids in the literature (Farmer et al. 2016; Xin et al. 2023, 2025), thereby providing a robust baseline for evaluating the impact of nuclear decay rate uncertainties.

2.1.2. Nuclear Network and Decay Rates

To accurately track energy generation and nucleosynthesis throughout the stellar lifetime and the subsequent explosion, we employ a dedicated nuclear reaction network coupled directly to the stellar structure equations. We utilize a custom 162-isotope network, referred to as `mesa162.net`, which is an extension of the standard `mesa_161.net`. The detailed list of isotopes included in the network is provided in Table 1.

A distinguishing feature of our network is the explicit treatment of the ^{26}Al branched decay. Rather than treating ^{26}Al as a single species, we separate it into its ground state $^{26}\text{Al}^g$ ($J^{\pi} = 5^+$, $t_{1/2} = 7.17 \times 10^5$

Table 1. Isotopes Included in the Nuclear Reaction Network

Element	Mass Numbers (A)	Element	Mass Numbers (A)
n	1	S	31–35
H	1, 2	Cl	35–38
He	3, 4	Ar	35–40
Li	7	K	39–44
Be	7, 9, 10	Ca	39–46
B	8, 10, 11	Sc	43–48
C	12, 13	Ti	43–51
N	13–15	V	47–53
O	14–18	Cr	47–57
F	17–19	Mn	51–57
Ne	18–22	Fe	51–61
Na	21–24	Co	55–63
Mg	23–26	Ni	55–64
Al	25, 26 ^a , 27, 28	Cu	59–64
Si	27–31	Zn	60–64
P	30–33		

^aThe network explicitly treats the ground state ($^{26}\text{Al}^g$) and the isomeric state ($^{26}\text{Al}^m$) as separate species.

yr) and its short-lived metastable isomeric state $^{26}\text{Al}^m$ ($J^\pi = 0^+$, $t_{1/2} = 6.35$ s). These states are coupled via temperature-dependent internal transitions, allowing our models to self-consistently track the survival fraction of $^{26}\text{Al}^g$ under both hydrostatic and explosive conditions without relying on post-processing. For the iron-peak region, the network extends to ^{64}Zn , specifically encompassing isotopes from ^{51}Fe to ^{61}Fe and ^{55}Co to ^{63}Co to ensure a robust representation of the pathways leading to ^{60}Fe .

For computational efficiency during preliminary resolution sensitivity tests (Section 2.1.3), we utilize a smaller hardwired network, `approx21_cr60_plus_co56.net`, which has been extensively validated for massive star energetics (Weaver et al. 1978; Woosley & Weaver 1988; Heger et al. 2000; Heger & Woosley 2010; Chatzopoulos & Wheeler 2012; Farmer et al. 2016).

All reaction rates are drawn from JINA REACLIB (version 20171020; Cyburt et al. 2010) with the exception of the ^{59}Fe β^- decay rate. The ^{59}Fe β^- decay rate provided in JINA REACLIB is taken from LMP, which is widely adopted in stellar evolution and nucleosynthesis studies (e.g., Woosley et al. 2002; Paxton et al. 2011; Limongi & Chieffi 2018). However, recent experimental work by Gao et al. (2021) indicates that the decay rate is approximately three times higher than the

LMP estimate at temperatures relevant to C-shell burning ($T \approx 1.2$ GK) as shown in Figure 1. Regarding the production channel, we adopt the default $^{59}\text{Fe}(n, \gamma)^{60}\text{Fe}$ rate from JINA REACLIB for our entire model grid. Although recent experimental constraints on this neutron capture cross-section have emerged (Spyrou et al. 2024), we focus specifically on isolating the impact of the updated β^- decay rate in this work. Given that the yield of ^{60}Fe depends sensitively on the competition between these two channels, the systematic uncertainties associated with the neutron capture rate are further addressed in Section 4.3.4.

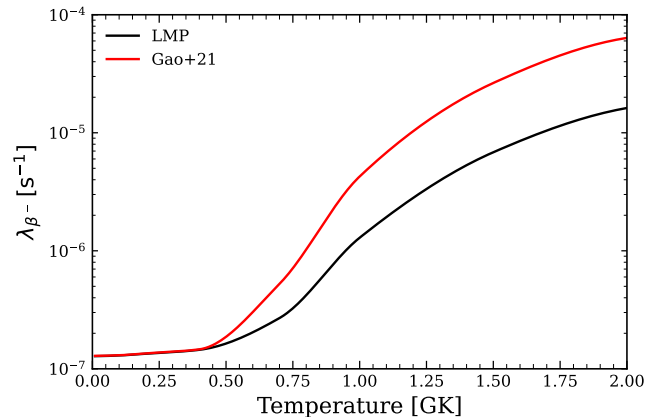


Figure 1. The β^- decay rate of ^{59}Fe as a function of temperature. The black line represents the widely used rates from Langanke & Martínez-Pinedo (2001), evaluated at a typical carbon-shell density of $\rho Y_e \approx 10^5 \text{ g cm}^{-3}$, while the red line shows the new rate from Gao et al. (2021). The temperature range is truncated at 2 GK, as the β^- decay channel becomes sub-dominant relative to the $^{59}\text{Fe}(p, n)^{59}\text{Co}$ reaction at higher temperatures.

2.1.3. Numerical Resolution Strategy

Reliable nucleosynthesis yields in massive stars require a fine-tuned balance between spatial and temporal resolution, particularly to resolve the thin burning shells and sharp composition gradients in advanced stages. We performed a comprehensive resolution sensitivity analysis focusing on two key MESA controls: the maximum fraction of a star’s mass in a cell, `max_dq` and the upper limit of the maximum allowed change in the central density between timesteps, `delta_lgRho_center_limit`.

We adopt a two-stage resolution strategy based on convergence tests across our mass range (15, 25, 40 M_\odot). For the evolution from ZAMS to helium depletion, we utilize a baseline resolution of `max_dq` = 1.0×10^{-3} and `delta_lgRho_center_limit` = 1.5×10^{-2} . Taking our 25 M_\odot model as a representative case, this setup typically yields a spatial grid of 2,000–3,000 mass shells, with

time steps ranging from $\sim 10^5$ yr during the main sequence to $\sim 10^2$ yr approaching helium depletion. This ensures that the helium core mass (M_{He}) converges within a 5% threshold. For the subsequent advanced burning stages until core collapse, we switch to a significantly finer resolution with `max_dq` = 5.0×10^{-4} and `delta_lgRho_center_limit` = 5.0×10^{-3} to capture the rapid structural changes and ensure a stable temperature profile at the onset of collapse. For the $25 M_{\odot}$ model, this enhanced resolution results in a grid of 4,000–5,000 mass shells, with time steps ranging from $\sim 10^2$ yr to as low as $\sim 10^{-8}$ yr (less than 1 second) to adaptively capture the rapid structural changes and convective episodes in the final stages. While the 25 and $40 M_{\odot}$ models show well-defined stability windows, we note that $15 M_{\odot}$ models exhibit a higher sensitivity to numerical choices, requiring a localized “island of stability” for consistent results.

This rigorous control is essential because the ^{60}Fe yield is extremely sensitive to the thermal structure of the carbon-burning shells. Our tests indicate that varying the resolution alone can induce yield fluctuations of up to 60%, which could potentially obscure the $\sim 40\%$ physical suppression expected from the updated ^{59}Fe decay rate (Gao et al. 2021). By prioritizing the convergence of the pre-supernova temperature profile, we ensure that the suppressed ^{60}Fe production observed in our grid is a robust physical response to the nuclear physics update rather than a numerical artifact.

Detailed methodologies, convergence diagnostics, and the results of our sensitivity grid are provided in Appendix A.

2.2. Core-collapse Supernovae

To simulate the hydrodynamic shock and explosive nucleosynthesis during the CCSN event, we utilize the `CCSN` module in `MESA` (modeled after the `example_ccsn_IIp` test suite) using a thermal bomb prescription as described below. Initially, we define the mass cut at an entropy of $S = 4 k_{\text{B}}$ baryon $^{-1}$ (Heger & Woosley 2010; Ertl et al. 2016). The material interior to this surface is excised from the computational domain and assumed to form the compact remnant. To initiate the explosion, we inject energy into a thin shell of $0.02 M_{\odot}$, so that the total energy of stars reaches 1×10^{51} erg (`inject_until_reach_model_with_total_energy` = 1.0×10^{51} erg). This approach ensures that the resulting explosion carries a prescribed net energy, accounting for the gravitational binding energy of the progenitor’s envelope. The energy is deposited over a characteristic

timescale of $t_{\text{inj}} = 5$ ms, launching a hydrodynamic shockwave that propagates outward.

As the shockwave traverses the stellar layers, explosive nucleosynthesis modifies the abundances of ^{26}Al and ^{60}Fe , primarily in the carbon-burning (C) shell where post-shock temperatures exceed 2×10^9 K (Limongi & Chieffi 2006). In this study, we define the “ejecta” as mass cells maintaining a positive total energy ($E_{\text{tot}} = E_{\text{kin}} + E_{\text{th}} + \Phi_{\text{grav}} > 0$). The simulation is terminated when the temperature of the innermost ejectable cell drops below 1.0×10^8 K. At this stage, the charged-particle reactions responsible for the production and destruction of ^{26}Al and ^{60}Fe have effectively frozen out, ensuring the final yields remain constant.

2.3. Galactic $^{60}\text{Fe}/^{26}\text{Al}$ Flux Ratio

To evaluate the collective impact of the updated ^{59}Fe decay rate at a Galactic scale, we employ an integration framework to estimate the Galactic γ -ray flux ratio, $I(^{60}\text{Fe})/I(^{26}\text{Al})$. Given that the half-lives of ^{26}Al ($t_{1/2} \approx 0.717$ Myr) and ^{60}Fe ($t_{1/2} \approx 2.62$ Myr) are several orders of magnitude shorter than the Galactic evolution timescale, we adopt the steady-state assumption where the total production and decay rates are balanced (e.g., Limongi & Chieffi 2006; Diehl et al. 2021). Assuming both isotopes originate from the same massive star populations, the averaged Galactic γ -ray flux ratio can be directly related to the ratio of their integrated Galactic yield rates:

$$\frac{I(^{60}\text{Fe})}{I(^{26}\text{Al})} \approx \frac{26}{60} \cdot \frac{\dot{M}_{\text{Gal}}(^{60}\text{Fe})}{\dot{M}_{\text{Gal}}(^{26}\text{Al})} \quad (1)$$

The integrated Galactic yield rate for each isotope is calculated by convolving our stellar yields with a normalized Initial Mass Function (IMF):

$$\dot{M}_{\text{Gal}} \propto \int_{M_{\text{min}}}^{M_{\text{max}}} Y(m) \cdot m^{-(1+x)} dm \quad (2)$$

where $Y(m)$ is the total net mass of the isotope ejected by a star of initial mass m over its entire lifetime. For ^{60}Fe , $Y(m)$ is derived from the core-collapse supernova (CCSN) ejecta. For ^{26}Al , $Y(m)$ represents the cumulative sum of the time-integrated stellar wind contribution and the explosive CCSN yield. In our calculations, the integration limits are set to $M_{\text{min}} = 14 M_{\odot}$ and $M_{\text{max}} = 80 M_{\odot}$, consistent with our `MESA` grid coverage. We adopt a baseline Salpeter IMF slope of $x = 1.35$ (Salpeter 1955) and further explore the sensitivity of the flux ratio by varying x from 0.5 to 2.5. This specific formulation allows us to isolate the influence of the nuclear reaction rates from complex Galactic transport effects, providing a direct measure of how the ^{59}Fe decay rate

propagates from a single stellar interior to observable Galactic signals.

3. RESULTS

We performed two parallel sets of stellar evolution and nucleosynthesis calculations for models with initial masses spanning 14 to $80 M_{\odot}$. Both grids utilize the extended `mesa_162.net` nuclear network, as detailed in Section 2.1.2. The first grid, hereafter the Default Rate (DR) series, employs the default ^{59}Fe β^- -decay rate from the LMP tables. The second grid, the New Rate (NR) series, incorporates the updated experimental rate from Gao et al. (2021). All other nuclear inputs, physical and numerical parameters remain identical between the two sets. This section presents the direct numerical outputs of our simulations and is organized as follows.

We first describe the general evolutionary properties of our models, focusing on the helium core masses (M_{He}) and central ^{12}C mass fractions at the end of core helium burning. We then present the yields for both ^{26}Al and ^{60}Fe , and trace how the updated ^{59}Fe decay rate influences the nucleosynthetic yields of ^{60}Fe , with the case pair of $30 M_{\odot}$ models. Finally, we present the resulting $^{60}\text{Fe}/^{26}\text{Al}$ flux ratios as a function of the IMF slope.

3.1. Basic Evolutionary Properties

Table 2 summarizes the fundamental evolutionary properties for both the DR and NR model grids. The table lists the initial (M_{ini}) and final (M_{fin}) stellar masses, alongside the structural parameters at helium depletion. We define helium depletion as the stage when the central helium mass fraction drops below $X_{\text{c}}(^4\text{He}) = 10^{-4}$. At this stage, we determine the dimensions of the helium core and the carbon-oxygen (CO) core based on chemical abundance criteria. Specifically, the helium core boundary is defined as the outermost coordinate where $X(^1\text{H}) < 1 \times 10^{-4}$. For WR stars, which have been stripped of their hydrogen envelopes via strong stellar winds, the helium core mass is effectively equivalent to the total stellar mass. Similarly, the CO core boundary is located where $X(^4\text{He})$ drops below 0.01 and either $X(^{12}\text{C})$ or $X(^{16}\text{O})$ exceeds 0.1. Additionally, we report the central mass fraction of ^{12}C at helium depletion.

Table 2 also reports the properties characterizing the CCSN explosions, including the initial mass cut (M_{cut}), defined at entropy $S = 4 k_{\text{B}}$ baryon $^{-1}$, the fallback mass (M_{fb}), the final remnant mass (M_{rem}), and the total ejecta mass (M_{ej}). Finally, the relevant timescales are provided, covering the lifetimes of hydrogen burning, helium burning, and the total stellar lifespan.

The helium core mass (M_{He}) and central mass fraction of ^{12}C are two primary determinants of the advanced evolutionary stages and the final nucleosynthetic

yields of massive stars (Chieffi & Limongi 2020; Xin et al. 2025). Figure 2 illustrates the relationship between M_{He} and the initial stellar mass (M_{ini}). We find that M_{He} exhibits a monotonic increase with M_{ini} across the entire range of 14– $40 M_{\odot}$. Notably, the M_{He} values from our DR and NR series are virtually identical, except the models with initial mass of $20 M_{\odot}$, though the discrepancy remains within the established numerical tolerance. Furthermore, both production series show excellent agreement with the median values from our resolution sensitivity tests (see Appendix A). All production models fall within the gray shaded region representing a $\pm 5\%$ deviation from the resolution baseline, thereby validating the numerical robustness of our expanded `mesa162.net` network.

To ensure our models are consistent with the broader literature, we compare our results against several grids calculated using different stellar evolution codes: the KEPLER progenitor models from Sukhbold et al. (2016) (S16); the FRANEC models from Chieffi & Limongi (2020) (C20); and MESA single-star models from Schneider et al. (2021) (S21), Farmer et al. (2023) (F23), and Xin et al. (2025) (X25). Specifically, the $M_{\text{He}}-M_{\text{ini}}$ relation in our grid demonstrates a high degree of conformity with the extensive progenitor sample from S16. C20 and F23 yield higher core masses, while X25 shows a lower trend; these differences primarily arise from differing treatments of convective overshooting and mass loss prescriptions. Overall, this consistent alignment provides a robust physical foundation for our subsequent yield analysis.

The central mass fraction of ^{12}C at central helium depletion is a key determinant of the subsequent shell-burning structures and nucleosynthesis yields. Tur et al. (2010) demonstrated that the triple- α and $^{12}\text{C}(\alpha, \gamma)^{16}\text{O}$ reaction rates influence the advanced burning stages and final yields of ^{60}Fe and ^{26}Al in a complex manner. In particular, the final yield of ^{60}Fe is highly sensitive to these rate uncertainties, potentially varying by a factor of 3–5 within their 1σ uncertainty limits, whereas the ^{26}Al yield is less sensitive to these reaction rates. Consequently, the central mass fraction of ^{12}C at helium depletion serves as a critical benchmark for validating the evolutionary baseline of our investigation into the nucleosynthesis of ^{60}Fe .

Here we also compare our results against the reference grids. Since the updated ^{59}Fe decay rate does not physically impact the core helium burning phase, the $X(^{12}\text{C})$ values between the DR and NR series are virtually identical, subject only to minor numerical fluctuations (see Table 2). For clarity, we only present the results of the DR models in Figure 3. The over-

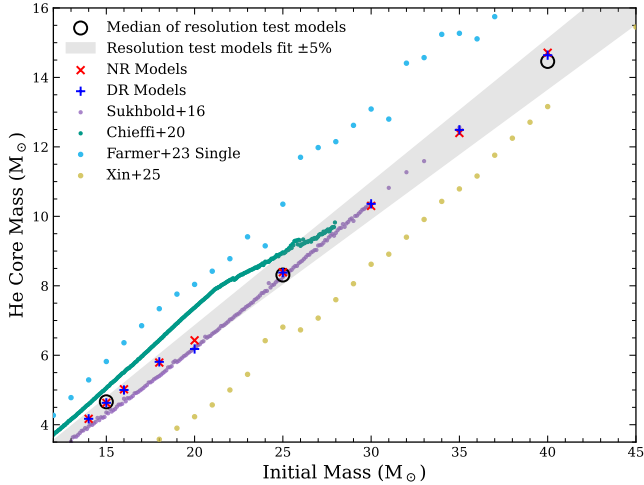


Figure 2. Comparison of helium core masses (M_{He}) as a function of initial stellar mass (M_{ini}). The gray shaded region delineates the $\pm 5\%$ convergence band derived from our resolution sensitivity analysis (Section 2.1.3). Our production models using both default (DR; blue pluses) and updated (NR; red crosses) ^{59}Fe decay rates are overlaid, showing no significant structural divergence. For benchmarking, we include data from progenitor models of Sukhbold et al. (2016), Chieffi & Limongi (2020), single-star models from Farmer et al. (2023), and Xin et al. (2025).

all trend of our models shows excellent agreement with other MESA-based results (S21 and F23). Notably, our carbon mass fractions, along with those from independent MESA models, are positioned between the higher values predicted by the FRANEC models (C20) and the lower values from the KEPLER models (S16). This well-constrained $X(^{12}\text{C})-M_{\text{ini}}$ relationship provides a reliable physical background for the subsequent shell burning and s-process nucleosynthesis of ^{60}Fe .

3.2. Nucleosynthetic Yields of ^{26}Al and ^{60}Fe

The nucleosynthetic yields for ^{26}Al and ^{60}Fe are detailed in Table 3. For each model, we report the final total ejected mass (M_{tot}) of each isotope, along with the contributions from three distinct sources: (1) stellar winds (relevant only for ^{26}Al), (2) the hydrostatic shell contribution before the explosion, and (3) the net contribution from explosive nucleosynthesis and fallback during the CCSN event.

The hydrostatic shell contribution is computed by integrating the isotopic abundances from the initial mass cut to the surface using the pre-supernova profiles. The net contribution from CCSN events is calculated by taking the difference between the final ejected mass and the pre-supernova inventory. This term accounts for the complex interplay between shock-induced synthesis and dynamic fallback. While the shock wave can synthesize

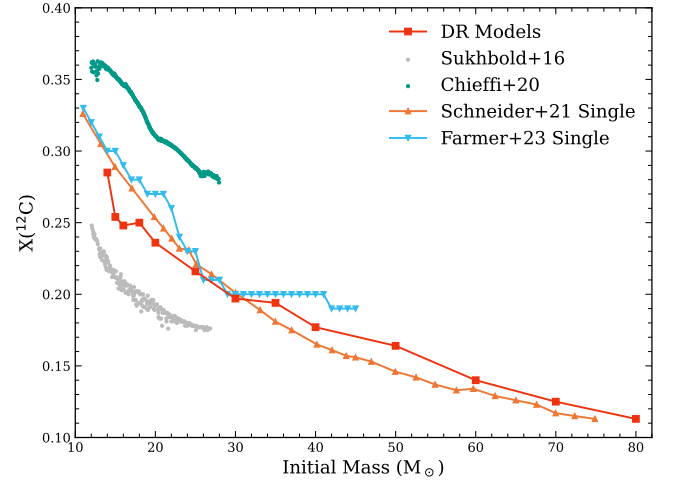


Figure 3. Comparison of ^{12}C mass fractions at central helium depletion. Red solid line with squares: DR models; grey dots: progenitor models from Sukhbold et al. (2016); green dots: Chieffi & Limongi (2020); orange solid line with triangles: single-star models from Schneider et al. (2021); light blue solid line with triangles: single-star models from Farmer et al. (2023).

new isotopes (or destroy existing ones via photodisintegration), a portion of the pre-existing material may fail to escape and instead fall back onto the compact remnant. Consequently, a positive sign indicates net production during the explosion, while a negative sign implies a net loss of the pre-existing isotopes, either due to nuclear destruction or sequestration via fallback.

We first examine the yields of ^{26}Al as a control case to quantify the intrinsic numerical fluctuations inherent in our 1D stellar models. Since the production channels of ^{26}Al are physically decoupled from the iron-peak weak interactions, its yields should, in principle, remain unaffected by the updated ^{59}Fe decay rate. As shown in Figures 4(a) and (d), the ^{26}Al yields remain robustly consistent across both the Default Rate (DR) and New Rate (NR) grids. To formally validate this, we calculated the logarithmic yield differences, $\Delta \log_{10} Y = \log_{10}(Y_{\text{NR}}) - \log_{10}(Y_{\text{DR}})$. A one-sample t -test on these differences yields $p = 0.457$, indicating that we cannot reject the null hypothesis of zero expected change. This confirms that the variations in ^{26}Al exhibit no systematic physical offset and are driven purely by stochastic numerical noise. Consequently, we adopt the standard deviation of these fluctuations ($\sigma_{\text{Al}} \approx 0.26$ dex) as the baseline numerical noise floor for our subsequent analysis.

In stark contrast, the nucleosynthesis of ^{60}Fe is profoundly impacted by the updated nuclear physics input. Figures 4(b) and (c) reveal a systematic suppression of

Table 2. Basic evolution properties of the stellar models

^{59}Fe decay rate	M_{ini}	M_{fin}	M_{He}	M_{CO}	M_{cut}	M_{fb}	M_{rem}	M_{ej}	$X(^{12}\text{C})$	τ_{H}	τ_{He}	τ_{total}
	(M_{\odot})	(M_{\odot})	(M_{\odot})	(M_{\odot})	(M_{\odot})	(M_{\odot})	(M_{\odot})	(M_{\odot})		(Myr)	(Myr)	(Myr)
DR	14	13.290	4.199	2.489	1.46	0.00	1.46	11.83	0.287	12.856	1.454	14.340
	15	12.910	4.663	2.888	1.57	0.00	1.57	11.34	0.257	11.700	1.364	13.088
	16	13.433	5.037	3.217	1.78	0.00	1.78	11.66	0.253	10.736	1.237	11.994
	18	14.367	5.847	3.909	1.49	0.00	1.49	12.87	0.247	9.303	1.034	10.354
	20	17.316	6.223	4.238	1.48	0.50	1.98	15.33	0.204	8.152	1.054	9.220
	25	19.789	8.423	6.231	1.58	0.52	2.10	17.69	0.214	6.430	0.724	7.164
	30	22.098	10.412	8.058	2.25	0.72	2.97	19.13	0.189	5.586	0.512	6.105
	35	23.310	12.551	10.003	1.97	2.97	4.94	18.37	0.190	4.882	0.529	5.417
	40	25.745	14.705	11.964	2.07	0.46	2.53	23.21	0.182	4.454	0.481	4.940
	50	33.245	19.011	15.891	1.72	0.95	2.66	30.58	0.175	3.895	0.415	4.314
	60	24.136	24.181	20.350	2.66	0.00	2.65	21.49	0.171	3.535	0.373	3.912
	70	32.927	30.608	26.945	2.19	22.80	24.99	7.94	0.122	3.284	0.359	3.646
	80	34.649	34.980	31.404	2.06	30.29	32.35	2.30	0.116	3.097	0.341	3.441
	NR	14	13.290	4.198	2.493	1.43	0.00	1.43	11.87	0.285	12.856	1.455
15		12.895	4.663	2.895	1.64	0.00	1.64	11.26	0.254	11.700	1.370	13.094
16		13.407	5.053	3.224	1.62	0.00	1.62	11.79	0.248	10.736	1.239	11.996
18		14.425	5.830	3.890	1.50	0.00	1.50	12.93	0.250	9.303	1.033	10.352
20		17.351	6.471	4.475	1.54	0.00	1.54	15.81	0.236	8.148	0.941	9.103
25		19.608	8.435	6.241	1.63	0.00	1.63	17.98	0.216	6.430	0.723	7.163
30		22.645	10.354	7.962	1.86	0.79	2.65	20.00	0.197	5.491	0.605	6.104
35		24.206	12.458	9.871	2.50	2.47	4.97	19.24	0.194	4.967	0.445	5.418
40		24.972	14.783	12.056	1.68	0.58	2.26	22.71	0.177	4.454	0.482	4.941
50		30.904	19.547	16.448	2.53	10.45	12.98	17.93	0.164	3.893	0.418	4.315
60		31.621	25.045	21.666	2.05	18.88	20.93	10.69	0.140	3.535	0.380	3.919
70		32.506	30.580	27.011	1.75	20.92	22.66	9.84	0.125	3.284	0.357	3.644
80		38.048	35.742	31.776	2.08	27.28	29.36	8.68	0.113	3.097	0.341	3.441

NOTE—All masses are given in solar units (M_{\odot}) and time in Myr. M_{ini} and M_{fin} are the initial and final stellar masses. M_{He} and M_{CO} denote the He-core and CO-core masses at helium depletion. M_{cut} is the initial mass cut at entropy $S = 4 k_{\text{B}}$ baryon $^{-1}$. M_{fb} and M_{rem} represent the fallback mass and final remnant mass, respectively, while M_{ej} is the total ejecta mass. $X_{\text{c}}(^{12}\text{C})$ is the central carbon mass fraction at helium depletion.

^{60}Fe yields in the NR models (red lines) compared to the DR models (blue lines). When analyzing the full mass range, the mean physical signal of ^{60}Fe reduction is partially obscured by background noise (SNR ≈ 0.95), primarily due to the extreme massive end of our grid ($M_{\text{ini}} \geq 60 M_{\odot}$). In these cases, both model series exhibit a sharp decline in yields due to substantial fallback during the CCSN explosion. In this fallback-dominated regime, the final yields are heavily dictated by explosion dynamics rather than nucleosynthesis processes. By focusing on the models less affected by fallback, the physical signal of ^{60}Fe suppression strengthens to a mean difference of $\Delta \log_{10} Y(\text{Fe}) \approx -0.33$ dex, resulting in an improved signal-to-noise ratio of SNR = 1.27. This

demonstrates that the suppression of ^{60}Fe successfully penetrates the 1σ numerical noise floor of the models.

To statistically secure the significance of this suppression, we performed a paired t -test on the logarithmic yields of ^{60}Fe across the entire grid. The test yields a highly significant result ($t = -2.768$, $p = 0.017$), formally confirming that the reduction is a robust physical consequence of the modified ^{59}Fe decay rate rather than a numerical artifact. Quantitatively, this modification leads to an average systematic reduction of 0.28 dex ($\sim 48\%$) in the total ^{60}Fe yields, with the effect being more pronounced (0.33 dex, or $\sim 53\%$) when excluding fallback-dominated cases. This systematic offset suggests that the enhanced β^{-} decay of ^{59}Fe acts as a pri-

Table 3. ^{26}Al and ^{60}Fe yields

^{59}Fe decay rate	M_{ini}	^{26}Al Yields				^{60}Fe Yields		
		M_{tot}	M_{wind}	M_{sh}	M_{exp}	M_{tot}	M_{sh}	M_{exp}
	(M_{\odot})	(M_{\odot})	(M_{\odot})	(M_{\odot})	(M_{\odot})	(M_{\odot})	(M_{\odot})	(M_{\odot})
DR	14	3.99(-05)	4.37(-09)	2.24(-05)	+1.75(-05)	3.05(-05)	8.82(-06)	+2.17(-05)
	15	2.23(-05)	1.42(-09)	1.98(-05)	+2.47(-06)	5.47(-05)	2.24(-05)	+3.23(-05)
	16	4.70(-05)	2.40(-09)	7.13(-05)	-2.43(-05)	2.68(-05)	4.30(-05)	-1.62(-05)
	18	3.13(-05)	1.04(-08)	1.30(-05)	+1.83(-05)	1.60(-05)	1.76(-05)	-1.58(-06)
	20	5.47(-05)	1.42(-07)	2.86(-05)	+2.60(-05)	3.75(-05)	5.41(-05)	-1.66(-05)
	25	8.79(-05)	5.48(-07)	4.44(-05)	+4.30(-05)	5.21(-05)	4.37(-05)	+8.43(-06)
	30	1.90(-04)	1.62(-06)	2.42(-04)	-5.35(-05)	1.20(-04)	1.41(-04)	-2.07(-05)
	35	7.88(-05)	3.03(-06)	9.73(-05)	-2.15(-05)	1.66(-04)	1.74(-04)	-7.32(-06)
	40	2.27(-04)	4.46(-06)	2.25(-04)	-2.72(-06)	2.26(-04)	2.34(-04)	-8.17(-06)
	50	1.57(-04)	7.18(-06)	1.26(-04)	+2.36(-05)	1.64(-04)	1.64(-04)	+1.43(-07)
	60	4.15(-04)	4.68(-05)	5.34(-04)	-1.66(-04)	2.41(-04)	2.64(-04)	-2.23(-05)
	70	4.92(-04)	5.37(-05)	1.75(-04)	+2.63(-04)	6.18(-05)	1.47(-04)	-8.48(-05)
80	1.07(-04)	9.10(-05)	8.69(-05)	-7.14(-05)	1.58(-05)	1.15(-04)	-9.90(-05)	
NR	14	2.07(-05)	4.38(-09)	1.78(-05)	+2.89(-06)	3.22(-06)	3.83(-06)	-6.09(-07)
	15	1.21(-05)	1.16(-09)	1.37(-05)	-1.65(-06)	4.55(-05)	1.87(-05)	+2.69(-05)
	16	2.96(-05)	2.55(-09)	2.06(-05)	+8.95(-06)	2.07(-05)	2.59(-06)	+1.81(-05)
	18	3.43(-05)	8.88(-09)	1.24(-05)	+2.19(-05)	9.92(-06)	1.07(-05)	-7.58(-07)
	20	9.29(-05)	8.57(-08)	8.62(-05)	+6.64(-06)	6.68(-06)	7.20(-06)	-5.14(-07)
	25	7.74(-05)	5.26(-07)	3.26(-05)	+4.43(-05)	4.46(-05)	4.65(-05)	-1.85(-06)
	30	1.20(-04)	1.20(-06)	8.16(-05)	+3.75(-05)	9.33(-05)	9.89(-05)	-5.59(-06)
	35	2.62(-04)	2.27(-06)	4.00(-04)	-1.40(-04)	7.77(-05)	9.34(-05)	-1.57(-05)
	40	9.14(-05)	5.23(-06)	5.84(-05)	+2.78(-05)	5.18(-05)	5.16(-05)	+1.78(-07)
	50	1.45(-04)	8.52(-06)	1.97(-04)	-6.06(-05)	1.50(-04)	1.86(-04)	-3.55(-05)
	60	5.65(-04)	2.68(-05)	2.35(-04)	+3.03(-04)	5.31(-05)	1.32(-04)	-7.90(-05)
	70	1.19(-04)	5.58(-05)	1.23(-04)	-6.02(-05)	6.86(-05)	1.21(-04)	-5.26(-05)
80	2.01(-04)	7.27(-05)	6.20(-05)	+6.58(-05)	2.99(-05)	7.88(-05)	-4.89(-05)	

NOTE—All yields are given in solar masses (M_{\odot}). Parentheses denote powers of ten, where $A(B)$ signifies $A \times 10^B$ (e.g., $2.06(-04) = 2.06 \times 10^{-4}$). M_{tot} is the sum of wind, shell, and explosive components. For M_{exp} , a positive value indicates net production, while a negative value implies net decrease after explosion.

primary mechanism for suppressing ^{60}Fe production during convective shell burning. However, we note that the overall reduction in the ^{60}Fe yield could be more modest than indicated by our current models when considering competing effects, such as the recently measured enhancement in the $^{59}\text{Fe}(n, \gamma)^{60}\text{Fe}$ capture rate (Spyrou et al. 2024). The net impact on the Galactic $^{60}\text{Fe}/^{26}\text{Al}$ ratio thus remains subject to future multi-channel sensitivity tests that incorporate all updated nuclear data.

3.3. Physics of the Suppression: The $30 M_{\odot}$ Case

To elucidate the physical mechanism driving this suppression, we specifically examine the internal evolution

of the $30 M_{\odot}$ model. We select this mass as a representative case because it effectively captures the interplay between the weak interaction rates and stellar structure without the complicating effects of fallback dominance found in higher masses.

As detailed in previous studies (Limongi & Chieffi 2006; Diehl et al. 2021), ^{60}Fe production is governed by the neutron capture sequences during the He and C burning phases, especially within the convective shells. During He burning, temperatures typically remain below 0.5 GK. In this regime, both the LMP and the updated decay rates are consistently low (see Figure 1), implying minimal impact from the new nuclear data.

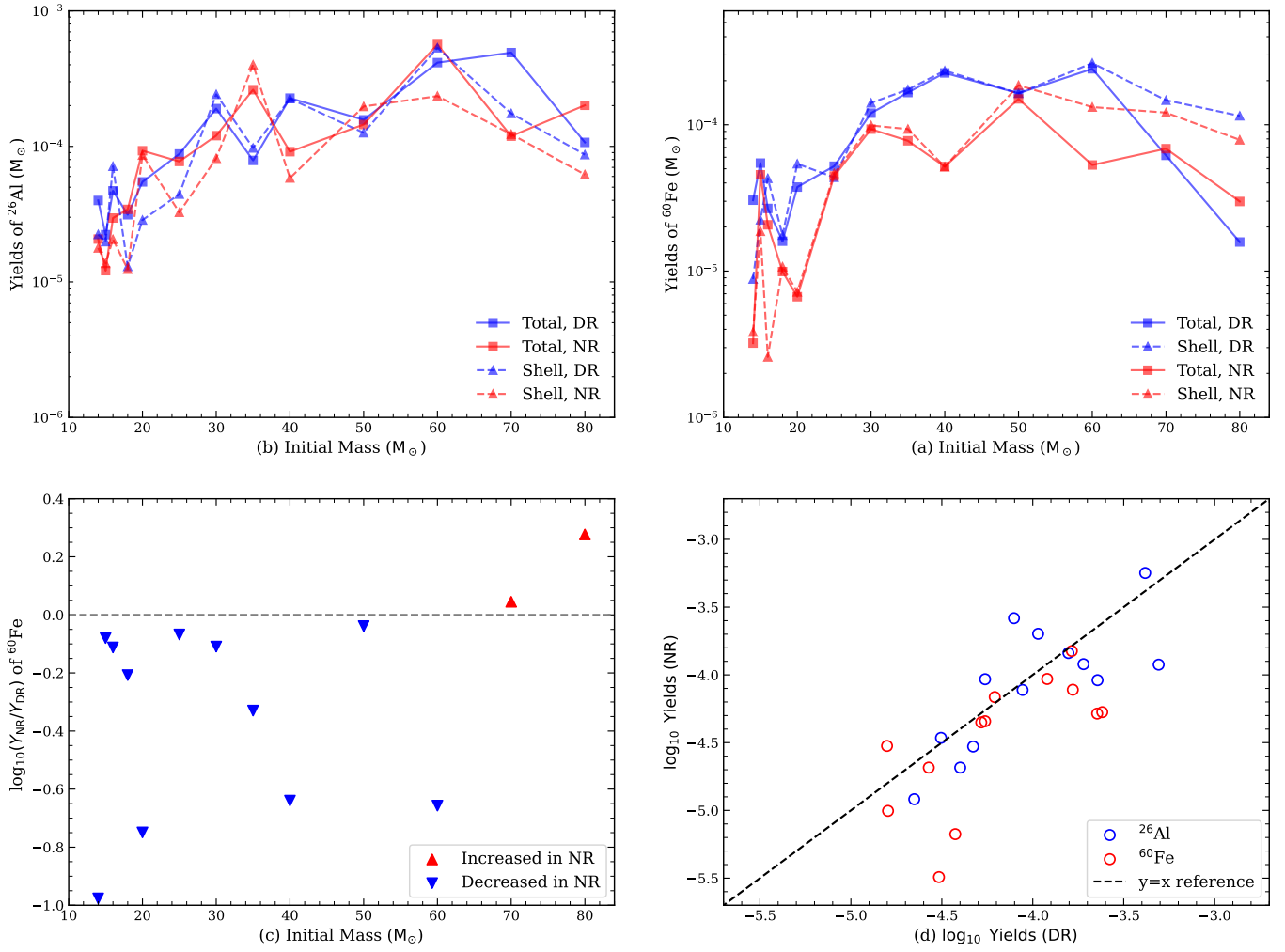


Figure 4. Nucleosynthesis yields of ^{26}Al and ^{60}Fe as a function of initial mass (14–80 M_{\odot}). (a, b) Comparison of yields between models using the default rate (DR, blue lines) and the updated rate (NR, red lines). Solid lines represent total yields, while dashed lines indicate pre-supernova hydrostatic shell yields. (c) The logarithmic ratio of ^{60}Fe total yields ($\log_{10}(Y_{\text{NR}}/Y_{\text{DR}})$), highlighting the substantial suppression of production in the NR models. (d) Direct comparison of yields relative to the identity line ($y = x$). Note the distinct response to the rate update: while ^{60}Fe (squares) exhibits a systematic reduction, ^{26}Al (circles) shows only random fluctuations.

However, at the higher temperatures characteristic of C-shell burning ($T \gtrsim 1.0\text{GK}$), the updated rate becomes significantly faster than the LMP prediction, creating a potent "leak" in the s-process path that suppresses the final ^{60}Fe yield.

3.3.1. Temporal Evolution

Figure 5 illustrates this mechanism by tracking the cumulative ^{60}Fe mass alongside the internal convective history. As shown by the solid lines, the accumulation tracks for the DR (black) and NR (red) models are identical during the early evolutionary phases ($\log(\tau_{\text{cc}} - t) \gtrsim 1$). This confirms that during helium burning, the difference in decay rates is negligible, resulting in identical nucleosynthetic paths.

A significant divergence emerges during the advanced stages, concomitant with the onset of convective carbon shell burning. In both models, the total ^{60}Fe yield increases rapidly as the carbon shell develops, driven by the activation of the $^{22}\text{Ne}(\alpha, n)^{25}\text{Mg}$ neutron source. However, the NR model exhibits a markedly slower growth rate due to the enhanced decay of the precursor ^{59}Fe . As the fuel and neutron source are consumed, the total ^{60}Fe yield in both models reaches a plateau prior to core silicon burning. Ultimately, the enhanced decay rate in the NR model leads to a final reduction of approximately 30% compared to the DR model.

3.3.2. Spatial Structure and Explosive Modification

The impact of the updated ^{59}Fe decay rate on the spatial distribution of ^{60}Fe is presented in Figure 6, which

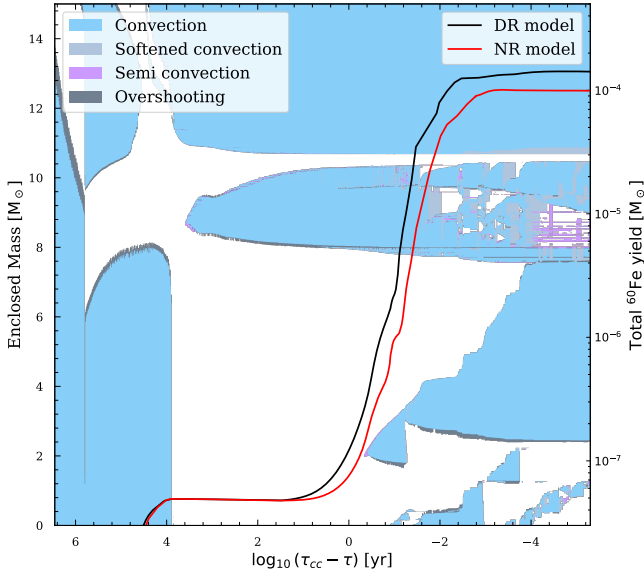


Figure 5. Evolutionary history of the $30 M_{\odot}$ model. The background Kippenhahn diagram (left axis) illustrates the internal structure evolution, showing convective (light blue), semi-convective (purple), and overshooting (dark gray) zones as a function of the logarithmic time remaining until core collapse ($\tau_{cc} - \tau$). The overlaid solid lines (right axis) track the cumulative ^{60}Fe mass yield. The black line represents the Default Rate (DR) model, while the red line indicates the New Rate (NR) model. Note that the deviation in ^{60}Fe production between the two models becomes prominent during the late evolutionary stages (e.g., carbon burning).

compares the internal mass fraction profiles before (top panels) and after (bottom panels) the supernova explosion. The top panels reveal that while the bulk shell structure remains robust against the rate update, the ^{60}Fe abundance is significantly altered. Specifically, in the DR model (top left), the ^{60}Fe mass fraction remains above 10^{-5} (grey dashed line) across a wide range of the O/Ne and He shells, with a distinct peak at the He/O shell boundary. In contrast, the NR model exhibits systematically lower abundances throughout these layers, directly reflecting the suppressed hydrostatic accumulation discussed above.

To further elucidate the spatial origin of this suppression, we decomposed the total pre-supernova ^{60}Fe yields (M_{sh} of ^{60}Fe Yields in Table 3) into contributions from the C-burning shell and the He-burning shell. Across our entire model grid, the He shell contributes an average of $\sim 26\%$ to the total ^{60}Fe inventory, although this fraction varies significantly with initial mass (ranging from nearly 0% to almost 80%). Statistical analysis reveals a clear site-specific sensitivity to the updated nuclear data: the ^{60}Fe produced in the C-burning shell, where temperatures reach $T \approx 1.2$ GK, exhibits a sig-

nificant systematic reduction of approximately 0.38 dex ($p = 0.017$, paired t -test) in the NR grid. Conversely, the ^{60}Fe abundance in the He-shell remains virtually unaffected by the rate update, showing no statistically significant offset. This disparity confirms that the global suppression of ^{60}Fe is primarily driven by the enhanced decay of ^{59}Fe in the high temperature environment of the C-shell, while the He-shell provides a stable component.

The bottom panels illustrate the modifications induced by the supernova shock. We observe that the passage of the shock wave results in largely minor changes to the global ^{60}Fe profile, except at the very base of the ejecta. Here, the high post-shock temperatures trigger the photodisintegration of ^{60}Fe into lighter species via (γ, n) reactions, and the reaction $^{60}\text{Fe}(p, n)^{60}\text{Co}$ can further deplete the abundance. Although a minor peak corresponding to explosive production is visible, it is outweighed by the destruction process. Consequently, for the $30 M_{\odot}$ model, the net contribution from the explosion is negative (as listed in Table 3). This balance between explosive production and destruction varies across the model grid and is inherently sensitive to the assumed explosion properties. While we adopt a uniform explosion energy of 10^{51} erg (1 foe) for all models, the peak post-shock temperatures, and thus the extent of ^{60}Fe destruction would scale with the explosion energy. The systematic uncertainties associated with this simplified explosion prescription and its impact on the final yields are further addressed in Section 4.3.

3.4. Galactic $^{60}\text{Fe}/^{26}\text{Al}$ Flux Ratio

Based on the integration framework outlined in Section 2, we predict the Galactic γ -ray flux ratio, $I(^{60}\text{Fe})/I(^{26}\text{Al})$, utilizing our computed stellar yields. Figure 7 compares these predictions against the observational constraint of 0.184 ± 0.042 , derived from INTEGRAL observations using a parameterized spatial morphology model (Wang et al. 2020). While we adopt this value as our primary benchmark, we note that observational estimates can range from 0.2 to 0.4 depending on the assumed spatial distributions of the two isotopes. A more detailed evaluation of these observational uncertainties is provided in Section 4.2.

Assuming a standard Salpeter IMF slope of $x = 1.35$, the DR models (blue line) predict a flux ratio of ~ 0.32 , which systematically overestimates the observed value, consistent with previous theoretical studies. In contrast, the NR models (red line), incorporating the updated reaction rate, yield a significantly reduced ratio of ~ 0.18 . This value is in excellent agreement with the observational limits.

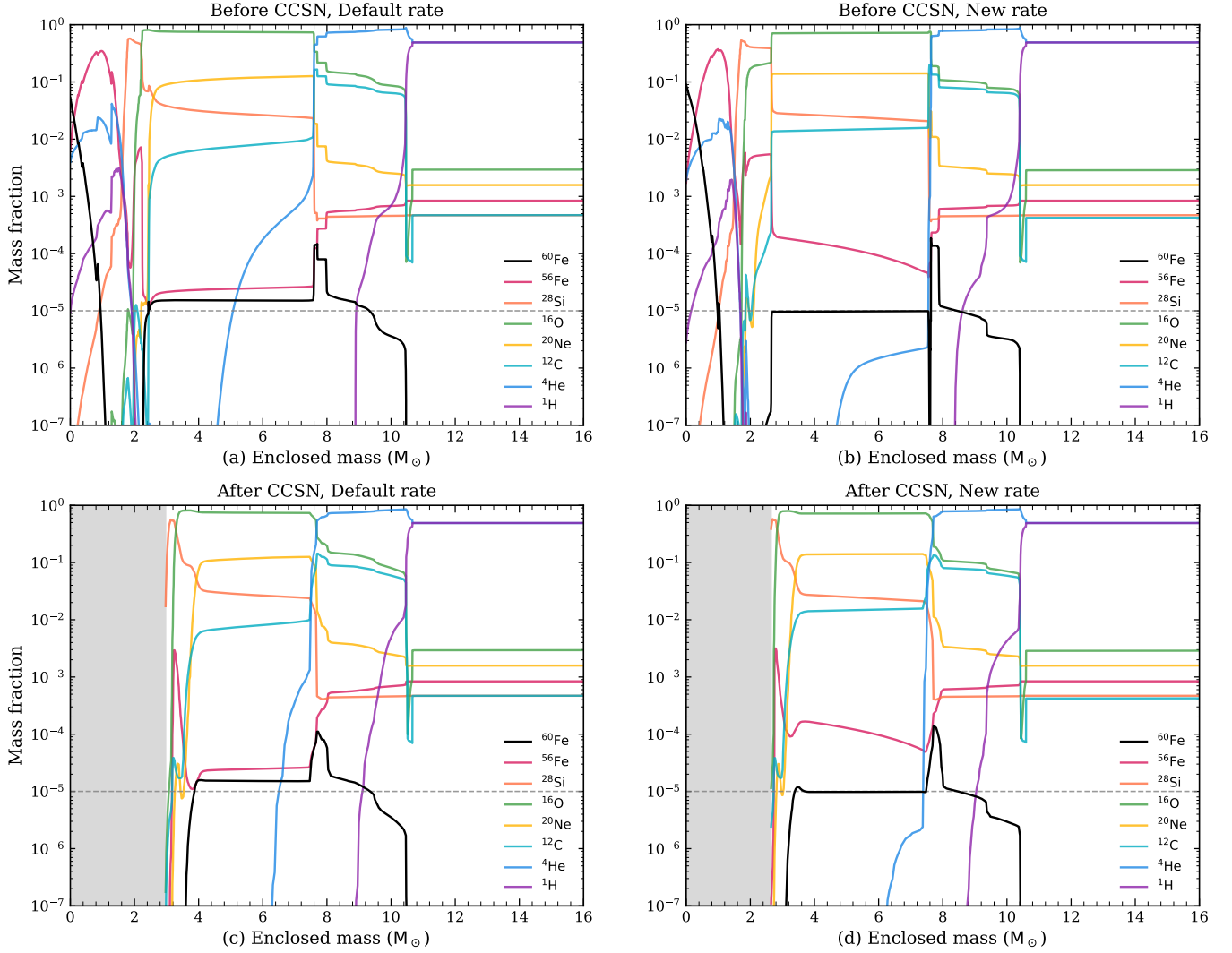


Figure 6. Internal mass fraction profiles of key isotopes (^1H , ^4He , ^{12}C , ^{16}O , ^{20}Ne , ^{28}Si , ^{56}Fe , and ^{60}Fe) for the $30 M_{\odot}$ models. The left panels (a, c) correspond to the Default Rate (DR) case, while the right panels (b, d) represent the New Rate (NR) case. Top panels show the pre-supernova stage, and bottom panels display the post-explosion distribution. The ^{60}Fe abundance is highlighted by the solid black line, with a horizontal dashed gray line at $X = 10^{-5}$ provided for visual reference. The gray shaded regions in the bottom panels denote the mass enclosed within the compact remnant and the fallback material ($M < M_{\text{cut}} + M_{\text{fb}}$), which is excluded from the final ejecta.

Notably, the predicted flux ratio exhibits a weak dependence on the IMF slope parameter x . As shown in Figure 7, the ratio remains relatively stable across a wide range of x values ($0.5 \leq x \leq 2.5$), with variations of less than ~ 0.05 .

The weak dependence of the integrated flux ratio on the IMF slope x can be attributed to the yield distribution across our model grid. Specifically, the $16\text{--}50 M_{\odot}$ mass range represents the dominant source for Galactic ^{60}Fe and ^{26}Al , consistently accounting for approximately 70% of the total integrated flux regardless of the chosen x value ($0.5 \leq x \leq 2.5$). Within this bulk population, the single-star $^{60}\text{Fe}/^{26}\text{Al}$ ratios remain rela-

tively stable, effectively anchoring the Galactic average. Furthermore, in IMF scenarios with small x , one might expect the most massive stars to significantly shift the ratio with their high $^{60}\text{Fe}/^{26}\text{Al}$ yields. However, in our models, stars with $M_{\text{ini}} \geq 60 M_{\odot}$ undergo substantial fallback during the supernova explosion with the applied explosion energy. This process traps a large fraction of the ^{60}Fe produced in the inner layers, preventing these very massive stars from exhibiting the high $^{60}\text{Fe}/^{26}\text{Al}$ ratios that would otherwise inflate the integrated result. Consequently, the Galactic flux ratio is robustly determined by the dominant intermediate mass population,

making it largely insensitive to the specific choice of IMF parameters.

However, we caution against overinterpreting the apparent alignment between our NR prediction (≈ 0.18) and the observational central value (0.184). Given the systematic uncertainties remaining in both stellar modeling and γ -ray data analysis, this excellent agreement may be partly fortuitous. Consequently, rather than serving as a final confirmation, this consistency and the IMF insensitivity underscore the need for a critical assessment of the underlying uncertainties, which we address in detail in Section 4.

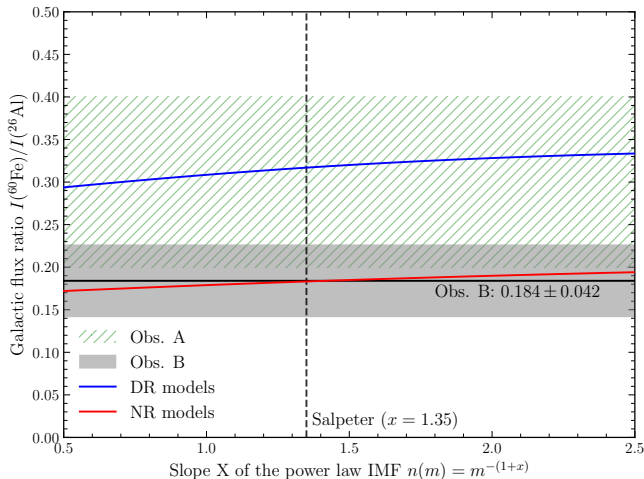


Figure 7. Predicted Galactic γ -ray flux ratio $I(^{60}\text{Fe})/I(^{26}\text{Al})$ as a function of the IMF slope parameter x . Results are shown for models with default ^{59}Fe decay rates (DR, blue line) and updated decay rates (NR, red line). The gray shaded region (Obs. B) and green hatched area (Obs. A) denote the observational constraints from the exponential disk model (0.184 ± 0.042) and various spatial morphology models, both derived from INTEGRAL data by Wang et al. (2020). For reference, the horizontal solid line marks the observed central value of 0.184, while the vertical dashed line marks the standard Salpeter IMF slope ($x = 1.35$).

4. DISCUSSION

Although our NR models incorporating the updated ^{59}Fe decay rate demonstrate the significant suppression of ^{60}Fe production and yield a galactic flux ratio consistent with observations, it is crucial to interpret these results within the context of model dependencies. In this section, we discuss the mass-dependent trends, compare our integrated results with observational constraints, and address the inherent systematic uncertainties.

4.1. Mass Dependence of the ^{60}Fe Yields and the Role of Fallback

The distinctive mass-dependent features of ^{60}Fe production are most prominent in the lower mass range ($M_{\text{ini}} < 50 M_{\odot}$). In this regime, the ^{60}Fe yields show a general upward trend with initial mass. However, detailed structure exists: the NR grid reveals a double-peak structure with maxima at $\sim 15 M_{\odot}$ and $\sim 30 M_{\odot}$, whereas the DR grid displays a single peak at $\sim 15 M_{\odot}$. Similar monotonic behavior with local variations has been reported in prior studies (Limongi & Chieffi 2006), although the exact peak locations differ. These shifts in peak positions likely reflect differences in underlying stellar physics assumptions (e.g., mass-loss rates and convective overshoot efficiencies) rather than the nuclear input alone. As analyzed in Section 3.4, this intermediate-mass range serves as the primary engine for Galactic enrichment, accounting for $\sim 70\%$ of the integrated flux ratio.

For high-mass stars, particularly those with $M_{\text{ini}} > 50 M_{\odot}$, a noticeable trend is the sharp decline in net ^{60}Fe yields. As shown in Figure 4(a), the final total yields (solid lines) in this regime tend to be lower than the pre-supernova hydrostatic contributions (dashed lines). This behavior contrasts with the findings of Limongi & Chieffi (2006) and Chieffi & Limongi (2013), who reported increasing net production with initial mass. This discrepancy arises from the different explosion prescriptions: while their models tune the explosion parameters to ensure the ejection of the entire mantle above the Fe-core regardless of initial mass, we adopt a standardized thermal bomb model with a fixed energy of 10^{51} erg across all masses. For very massive stars ($M_{\text{ini}} \gtrsim 50 M_{\odot}$), the increasing gravitational binding energy of the envelope leads to substantial fallback, preventing the ejection of the deep C/He-shell layers where ^{60}Fe is synthesized. In contrast, a posteriori mass cut determination in the Chieffi & Limongi (2013), which focuses on ^{56}Ni yields after ensuring mantle ejection, effectively bypasses the significant fallback. In our $70 M_{\odot}$ and $80 M_{\odot}$ models, the ejecta is dominated by the outermost layers, whereas the ^{60}Fe -rich regions almost entirely fall back onto the remnant. This retention of ^{60}Fe within the compact remnant in the high-mass regime effectively prevents these stars from dominating the integrated Galactic signal, even under top-heavy IMF assumptions.

It is worth noting, however, that our 1D hydrostatic treatment neglects multi-dimensional mixing processes, which naturally occur during shock propagation. In realistic multi-dimensional explosions, turbulent mixing can transport material from the deep interiors into

the outer envelope before fallback occurs. Such mixing would allow a fraction of the synthesized ^{60}Fe to be dredged up and ejected into the interstellar medium, thereby potentially increasing the integrated galactic yields and the resulting flux ratio.

This leads to a bifurcated conclusion regarding the mechanism of yield reduction. For lower to intermediate mass stars ($M_{\text{ini}} \lesssim 50 M_{\odot}$), the net loss of ^{60}Fe during the explosion is primarily governed by nuclear destruction via photodisintegration at the shock front. Conversely, for the high-mass regime ($M_{\text{ini}} > 50 M_{\odot}$), the fallback of deep, ^{60}Fe -rich layers onto the compact remnant becomes the dominant factor exacerbating the yield suppression. This dual-suppression mechanism ensures that the Galactic $^{60}\text{Fe}/^{26}\text{Al}$ ratio remains robustly anchored by the nucleosynthetic signature of the intermediate-mass population in our models.

4.2. Comparison with Galactic Observations

Interpreting the agreement between our models and observations requires careful consideration of the data analysis methods. While the galactic distribution of ^{26}Al is well-mapped, the specific morphology of ^{60}Fe emission remains poorly constrained (Diehl et al. 2021). Deriving a flux ratio from current data requires assuming a spatial tracer for the ^{60}Fe signal. Previous studies, and our work, often assume that ^{26}Al traces ^{60}Fe due to their shared origins in massive stars. However, Wang et al. (2020) demonstrated that different tracer maps lead to varying flux ratio estimates. Notably, they found that the ^{26}Al map is not the most statistically significant tracer for ^{60}Fe , suggesting that the two isotopes may have distinct spatial distributions.

Synthesizing results from various tracers, Wang et al. (2020) constrained the galactic flux ratio to the range of 0.2–0.4. In this context, our DR results (~ 0.32) fall comfortably within this window, while the NR result (~ 0.18) lies slightly below the lower bound. However, if considering the exponential disk model which yields 0.184 ± 0.042 , our NR prediction offers an excellent match. This comparison highlights that the tension between theory and observation is not solely a nuclear physics problem; it also stems from astrophysical and observational systematics.

Addressing these challenges requires a new generation of MeV γ -ray observatories with significantly improved sensitivity and spatial resolution. Upcoming and proposed missions offer a promising path to resolve these discrepancies. Specifically, The Compton Spectrometer and Imager project (COSI, Tomsick & COSI Collaboration 2022) is designed to provide high-resolution mapping of diffuse isotopic emission, aiming to perform

the first mapping of ^{60}Fe . Furthermore, proposed observatories such as (e-ASTROGAM, de Angelis et al. 2018) aim to provide detailed mapping of short-lived radioactivities, including both ^{26}Al and ^{60}Fe , while the All-sky Medium Energy γ -ray Observatory (AMEGO, McEnery et al. 2019) will offer advanced line sensitivity for nuclear lines such as the 1.8 MeV emission from ^{26}Al . These missions represent essential improvements in γ -ray instrumentation, providing the precision necessary to strictly constrain the key nucleosynthetic observable of the $^{60}\text{Fe}/^{26}\text{Al}$ flux ratio.

4.3. Systematic Uncertainties

Finally, we address the limitations inherent in our numerical approach and the physical assumptions adopted in this study.

4.3.1. Numerical Sensitivities

A primary challenge in modeling massive star nucleosynthesis is the sensitivity of the stellar structure to numerical resolution and physical assumptions. As noted in Section 2.1.3, we established a “stable island” in the parameter space where the pre-supernova structure converges robustly. This approach effectively mitigates numerical instabilities during the advanced burning stages. The robustness of this numerical framework is validated by the consistency of our ^{26}Al yields across different resolution sets, as well as the tight linear correlation maintained between the initial mass and the helium core mass. However, models around $15 M_{\odot}$ remain numerically sensitive, particularly regarding the temperature profiles of the inner shells (see Figure 9), which directly dictates the efficiency of ^{60}Fe synthesis. While we have demonstrated that the observed suppression of ^{60}Fe is a robust physical signal rather than a numerical artifact, the fluctuations in our control yields (e.g., ^{26}Al) suggest a persistent numerical noise floor of ~ 0.26 dex in absolute yield values.

4.3.2. Stellar Physics and Explosion Prescription

A primary source of systematic uncertainty stems from the 1D treatment of internal mixing. Our convection prescription relies on the 1D Mixing Length Theory, whereas convection in massive stars is inherently multi-dimensional. Consequently, while the relative suppression of ^{60}Fe due to the updated decay rate is a robust physical effect, the absolute yield values carry uncertainties inherent to 1D stellar evolution. Furthermore, stellar rotation, omitted in our current grid, is generally found to increase ^{26}Al yields due to enhanced mixing and mass loss, while also impacting ^{60}Fe production (Ekström et al. 2012; Limongi & Chieffi 2018; Brinkman et al. 2021; Falla et al. 2025).

Our explosion modeling is also simplified, adopting a uniform thermal bomb approach with a fixed energy of 1 foe. In reality, the explosion mechanism is still not fully understood, and the explosion energy likely scales with progenitor properties, which would in turn modify the shock-induced nucleosynthesis and the extent of fallback. This simplification likely contributes to the discrepancies in net explosive yields observed in our grid compared to previous studies. For instance, we do not observe the consistent net explosive production of ^{60}Fe and ^{26}Al across the entire mass range reported by Limongi & Chieffi (2006). Specifically, this leads to the mass-dependent bifurcation identified in our yields: for stars below $\sim 50 M_{\odot}$, the reduction in ^{60}Fe is primarily a result of shock-induced photodisintegration at the shell base. However, for more massive stars ($M > 50 M_{\odot}$), the suppression is significantly dominated by fallback, as the increasing gravitational binding energy of the progenitor exceeds our assumed 1 foe explosion energy. While a comprehensive exploration of explosion physics is beyond the scope of this work, we emphasize that the systematic suppression of ^{60}Fe in our models originates primarily in the hydrostatic C-shell. Therefore, this effect is expected to persist as a dominant correction regardless of the specific explosion model or energy adopted.

4.3.3. Incompleteness of Stellar Sources

Our current grid covers 14–80 M_{\odot} , leaving other potential sources and physical processes unaccounted for. First, we do not model the lower-mass end of massive stars (8–13 M_{\odot}). These stars are more numerous and are expected to produce a higher yield of ^{26}Al relative to ^{60}Fe (Limongi & Chieffi 2006; Brinkman et al. 2021), potentially lowering the integrated flux ratio further. Second, Asymptotic Giant Branch (AGB) stars are known contributors, though their ^{60}Fe yields remain highly uncertain, and both ^{26}Al and ^{60}Fe yields from AGB stars are considered to be subdominant compared to massive stars (Lugaro & Karakas 2008; Karakas 2010; Lugaro et al. 2018).

On the high-mass end (70–80 M_{\odot}), our models predict significant fallback, resulting in direct collapse to black holes and negligible contributions to the final yields. However, even for stars that fail to explode, a significant amount of ^{26}Al can be ejected via strong stellar winds during the Wolf-Rayet phase (Palacios et al. 2005). In contrast, ^{60}Fe is synthesized in deeper layers and remains retained in the compact remnant during fallback or collapse. This spatial decoupling would further suppress the integrated Galactic $^{60}\text{Fe}/^{26}\text{Al}$ ratio. We also note that we did not perform a self-consistent "explod-

ability" analysis (e.g., based on compactness parameters) (O'Connor & Ott 2011; Sukhbold & Woosley 2014; Ertl et al. 2016); the precise mass limits for successful supernovae remain an open question which could systematically shift the predicted flux ratio.

4.3.4. Nuclear Data Uncertainties

Beyond the ^{59}Fe decay rate, uncertainties in other key reaction rates persist. Recently, Spyrou et al. (2024) provided the most complete estimate on the $^{59}\text{Fe}(n, \gamma)^{60}\text{Fe}$ reaction using the β -Oslo method, which is 1.6 – 2.1 times higher than the previous estimation. While this significantly reduces the previously large uncertainty ($\sim 40\%$) associated with the production channel, it also implies an even higher potential for ^{60}Fe overproduction. Consequently, the final ^{60}Fe abundance remains critically sensitive to the balance between this neutron capture and the ^{59}Fe β^- -decay rate during shell burning. Additionally, for the decay rate of ^{60}Fe in stellar environments, discrepancies still exist between LMP and much earlier estimates (Fuller et al. 1982).

Meanwhile, the helium burning rate, the triple- α and $^{12}\text{C}(\alpha, \gamma)^{16}\text{O}$, introduces significant variations. Tur et al. (2010) demonstrated that these reaction rates influence the advanced burning stages and final yields in a complex manner; specifically, varying these rates within their 1σ uncertainty limits can lead to a factor of 3–5 variation in the final ^{60}Fe yield, whereas the ^{26}Al yield is notably less sensitive. While adjusting this rate could also align models with observations, it affects the entire structural evolution. Pignatari et al. (2013) also reported that the uncertainty in the $^{12}\text{C}+^{12}\text{C}$ reaction rate significantly influences the pre-explosive synthesis of ^{60}Fe and ^{26}Al . Furthermore, neutron source reactions, such as $^{22}\text{Ne}(\alpha, n)^{25}\text{Mg}$, are also crucial for overall ^{60}Fe yields and carry uncertainties. In contrast, the update to the ^{59}Fe β^- -decay rate provides a localized correction that systematically suppresses ^{60}Fe without requiring extreme variations in stellar structure.

Despite these remaining uncertainties, the crucial finding of this work stands: the updated ^{59}Fe β^- -decay rate introduces a systematic and significant suppression of ^{60}Fe production that is robust across the relevant mass range. By incorporating this updated nuclear physics, we identify a pivotal mechanism that significantly mitigates the long-standing overestimation of the galactic $^{60}\text{Fe}/^{26}\text{Al}$ flux ratio. This contribution moves theoretical predictions closer to the current observational limits, although a definitive resolution of the discrepancy will likely require the combined consideration of all newly available nuclear data across multiple reaction channels.

5. CONCLUSIONS

In this work, we performed a systematic investigation into the nucleosynthesis of the radioisotopes ^{26}Al and ^{60}Fe in massive stars, specifically focusing on the impact of the recently updated ^{59}Fe stellar β^- -decay rate. Using the MESA code, we constructed a grid of stellar evolution models ranging from 14 to $80 M_{\odot}$, coupled with a rigorous sensitivity analysis to ensure numerical stability. Our main conclusions are summarized as follows:

- Significant Suppression of ^{60}Fe :

Implementing the experimentally constrained ^{59}Fe decay rate (Gao et al. 2021) fundamentally alters the s-process path in massive stars. By enhancing the depletion of ^{59}Fe via β^- -decay, the new rate competes effectively with the neutron capture channel, particularly during convective Carbon shell burning. This leads to a global reduction in ^{60}Fe yields by approximately 0.28 dex ($\sim 47\%$) compared to models using the default LMP rate. This result suggests that previous nucleosynthesis models relying on theoretical rates have systematically overestimated the galactic ^{60}Fe production.

- Consistency with Galactic Observations:

The suppressed ^{60}Fe yields from our NR models lead to a predicted Galactic γ -ray flux ratio of $I(^{60}\text{Fe})/I(^{26}\text{Al}) \approx 0.18$. This value aligns closely with the observational constraint of 0.184 ± 0.042 derived from INTEGRAL data (Wang et al. 2020). However, as discussed in Section 4.3.4, the inclusion of the newly available experimental update for the $^{59}\text{Fe}(n, \gamma)$ capture rate (Spyrou et al. 2024), alongside future experimental constraints on other uncertain reactions, will provide further refinement to this theoretical prediction. Nevertheless, the observed weak dependence of this ratio on the IMF slope provides a robust theoretical baseline, suggesting that the β^- decay enhancement remains a key factor in mitigating the long-standing tension between theoretical yields and observational limits.

- Bifurcated Reduction Mechanism:

Contrary to previous studies where ^{60}Fe yields were often found to increase monotonically dur-

ing the explosion, we identified a mass-dependent bifurcation in the yield reduction mechanism, under the assumption of a uniform explosion energy of 1.0×10^{51} erg (1 foe) across our model grid. For intermediate-mass stars ($M \lesssim 50 M_{\odot}$), the yield reduction is primarily driven by shock-induced photodisintegration at the shell base. Conversely, for high-mass stars ($M > 50 M_{\odot}$), the suppression is dominated by significant fallback, as the increased gravitational binding energy outpaces the fixed explosion energy. While the identified bifurcation is framed within our current explosion modeling (see Section 4.3.2), the potential impacts of varied explosion energies and advanced explosibility criteria on the final ^{60}Fe and ^{26}Al yields remain compelling subjects for future systematic investigations.

ACKNOWLEDGMENTS

This work was supported by the National Natural Science Foundation of China under grant No.12588202, National Key R&D Program of China under grant No.2024YFA1611900, and Strategic Priority Research Program of Chinese Academy of Sciences under grant No.1160102. We thank Bingshui Gao for generously providing the experimental data on the ^{59}Fe β^- decay rate used in this work.

SOFTWARE AND DATA AVAILABILITY

The MESA configuration files (inlists), customized nuclear network, and experimental reaction rate tables required to reproduce the stellar evolution and nucleosynthesis simulations presented in this work are publicly available on Zenodo via the AAS Journals Community at [doi:10.5281/zenodo.20177425](https://doi.org/10.5281/zenodo.20177425). This Zenodo deposit also includes the stellar model properties (Table 2), isotopic yields (Table 3), and the Python-based analysis routines used for convolving yields with the IMF and generating Figure 7. For interactive viewing convenience, the analysis scripts and tabulated data are also mirrored on GitHub at <https://github.com/Tan-0321/Fe59-decay-impact-Fe60-Al26>.

APPENDIX

A. RESOLUTION SENSITIVITY AND NUMERICAL ROBUSTNESS

To ensure the robustness of our nucleosynthetic yields, we systematically investigated the impact of numerical resolution on core properties and stellar structure. This appendix details our convergence strategy and validates that our production models (using the extensive `mesa.162.net` network) reside within the numerically stable regime established by a dedicated test grid.

A.1. Methodology and Convergence Criteria

We constructed a test grid covering initial masses of $15 M_{\odot}$, $25 M_{\odot}$, and $40 M_{\odot}$ using the simplified `approx21_cr60_plus_co56.net` network. For each mass, we varied two key resolution control parameters: the maximum mass fraction change per cell (`max_dq`) and the temporal resolution control (`delta_lgrho_center_limit`).

A.1.1. Phase I: Helium Core Convergence

For the evolution from ZAMS to helium depletion, we focus on the convergence of the helium core mass (M_{He}). We define the percentage deviation as:

$$\delta M_{\text{He}} = \frac{M_{\text{He}}(\Delta m, \Delta t) - M_{\text{He}}^{\text{ref}}}{M_{\text{He}}^{\text{ref}}} \times 100\% \quad (\text{A1})$$

where $M_{\text{He}}^{\text{ref}}$ is the median value across the resolution grid. As shown in Figure 8, the timestep control (`delta_lgrho_center_limit`) is the dominant factor. We adopted a threshold of 5% (red dashed rectangle) to define our baseline resolution for the production run.

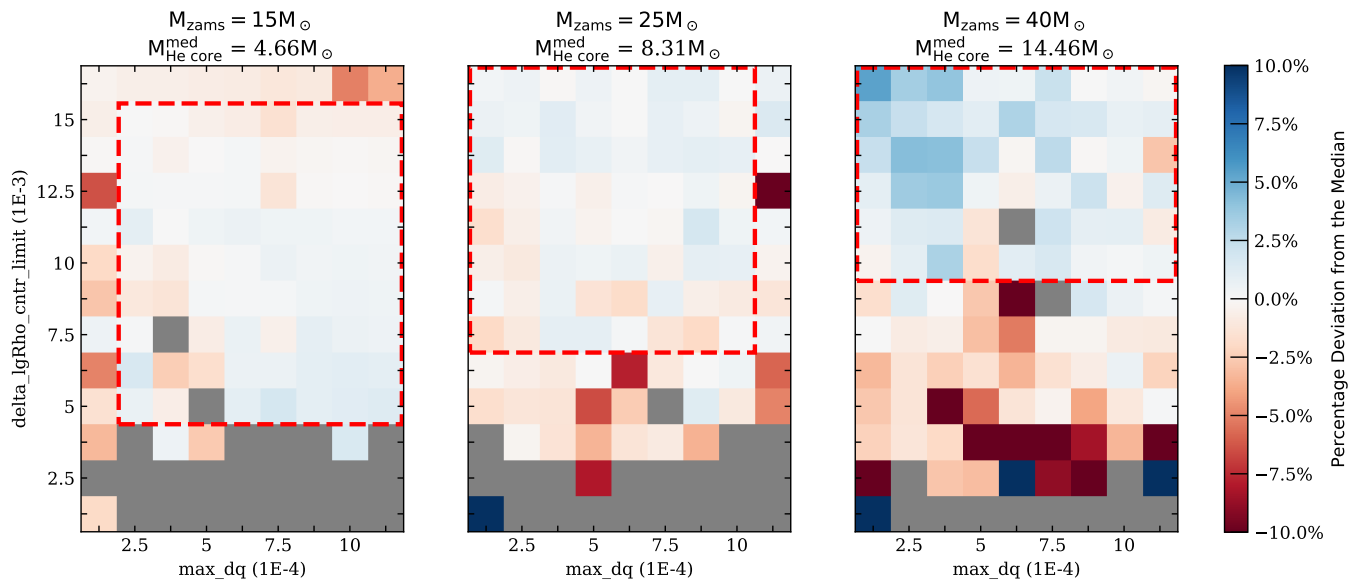


Figure 8. Percentage deviation of the helium core mass from the median value for models with 15, 25, and $40 M_{\odot}$. The red dashed rectangle highlights the region where deviation is $< 5\%$. Grey blocks indicate models that failed due to excessively small timesteps or convergence issues.

A.1.2. Phase II: Pre-Supernova Thermal Structure

For the advanced burning stages (post-helium depletion), we prioritize the stability of the temperature profile. We define the maximum absolute percentage deviation of the temperature profile just before iron core infall ($\log T_c \approx 9.85$) as:

$$D_{\text{temp}}^{\text{max}} = \max_m \left\{ \left| \frac{T(m) - \bar{T}(m)}{\bar{T}(m)} \right| \times 100\% \right\} \quad (\text{A2})$$

where $\bar{T}(m)$ is the refined average profile. Figure 9 (bottom panels) shows the stability map. While 25 and 40 M_{\odot} models show broad stability windows, the 15 M_{\odot} models are more stochastic. We selected resolution settings within the blue dashed “stability islands” ($D_{\text{temp}}^{\text{max}} < 20\%$) for our production runs.

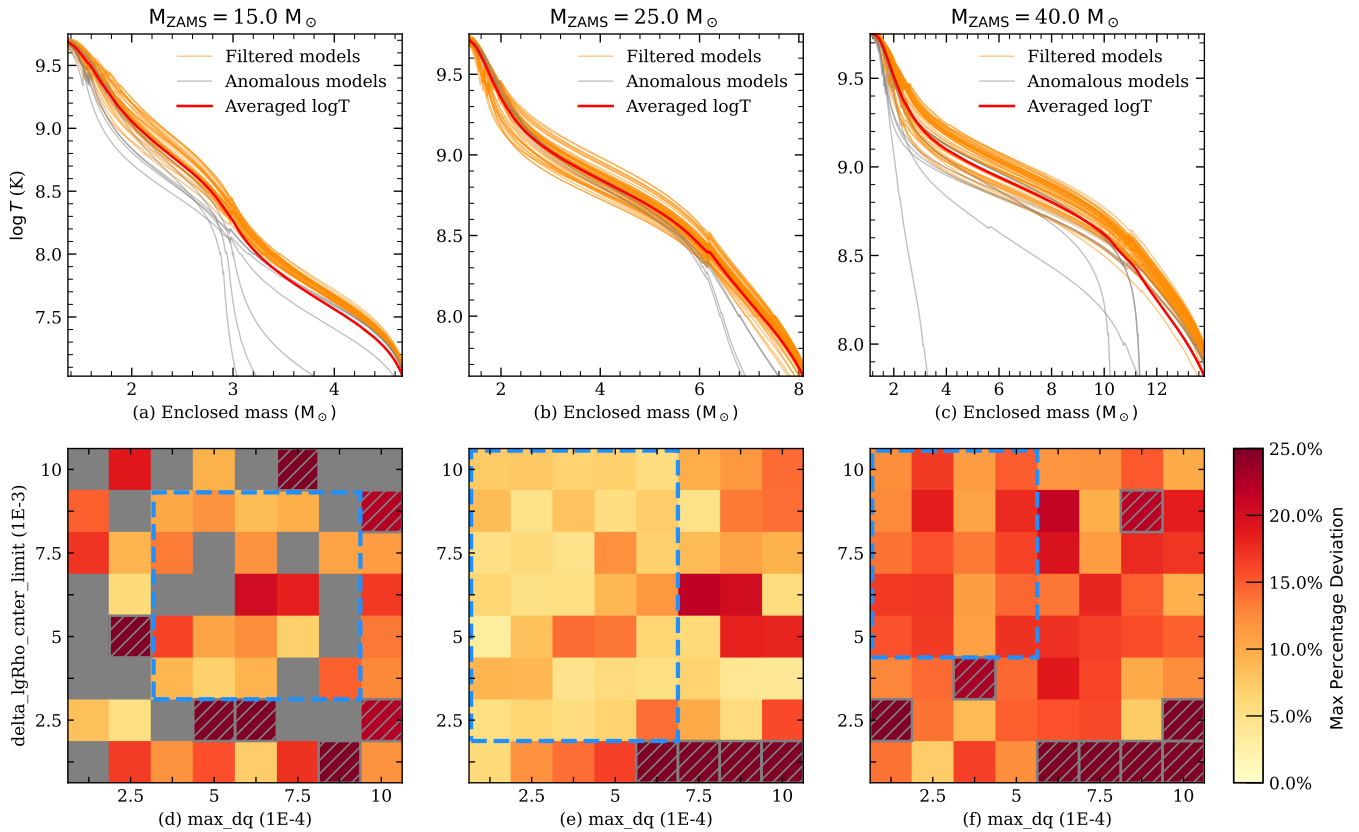


Figure 9. Resolution sensitivity analysis for advanced burning stages. **Top:** Temperature profiles prior to iron core infall. Grey curves are outliers ($> 50\%$ deviation), orange are valid models, and red is the average. **Bottom:** Map of maximum temperature deviation ($D_{\text{temp}}^{\text{max}}$). The blue dashed rectangles indicate the chosen stability parameters for production models.

A.2. Validation of Production Models

A critical step is to confirm that the resolution criteria derived from the test grid (small network) remain valid for the production grid (large network).

Structural Consistency—In Figure 2 (main text), we demonstrated that the helium core masses of our production models align perfectly with the test grid predictions and literature values.

Thermal Profile Consistency—Figure 10 compares the pre-supernova temperature profiles of the production models (using `mesa_162.net`) against the averaged profiles from the test grid. For the 15 and 25 M_{\odot} models, the production profiles fall well within the 20% deviation envelope (orange shaded region). The 40 M_{\odot} model shows a minor excursion near the C/Ne burning shell interface ($\sim 4 M_{\odot}$), which is a known region of high sensitivity to network-convection coupling. However, the overall thermal structure is preserved. This confirms that our two-stage resolution strategy provides a robust physical foundation for the nucleosynthesis analysis presented in this work.

REFERENCES

- Austin, S. M., West, C., & Heger, A. 2017, *ApJL*, 839, L9,
doi: [10.3847/2041-8213/aa68e7](https://doi.org/10.3847/2041-8213/aa68e7)
- Banerjee, P., Misch, G. W., Ghorui, S. K., & Sun, Y. 2018,
Phys. Rev. C, 97, 065807,
doi: [10.1103/PhysRevC.97.065807](https://doi.org/10.1103/PhysRevC.97.065807)

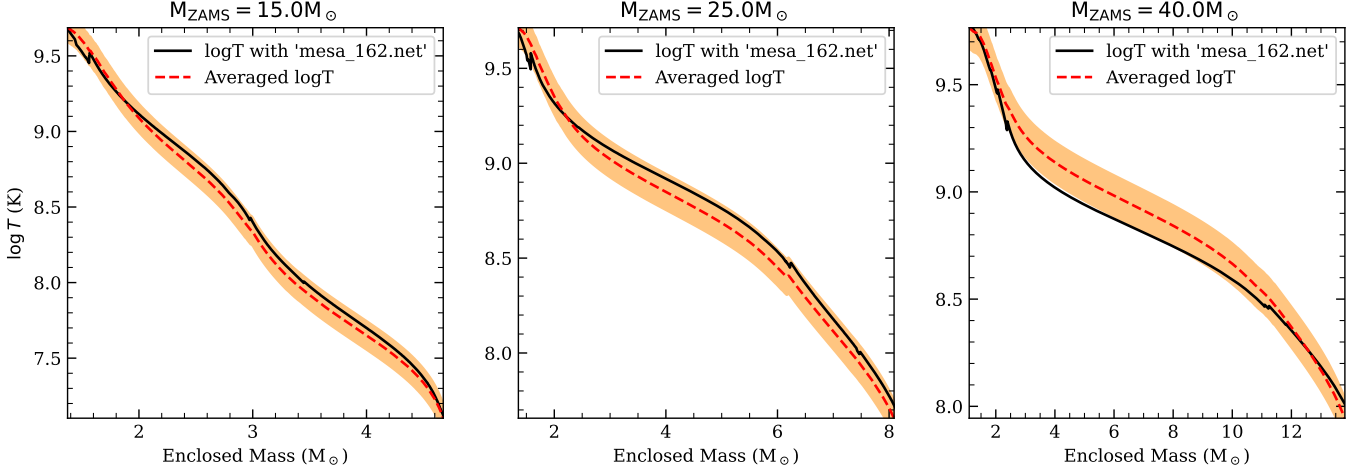


Figure 10. Validation of production models. Black lines show the temperature profiles of our production models (15, 25, 40 M_{\odot}) using the large network. Red dashed lines are the averaged profiles from the resolution test grid. Orange shaded regions indicate the $\pm 20\%$ deviation tolerance. Note the excellent agreement, confirming that network size does not induce significant structural drift.

- Bouchet, L., Jourdain, E., & Roques, J.-P. 2015, *ApJ*, 801, 142, doi: [10.1088/0004-637X/801/2/142](https://doi.org/10.1088/0004-637X/801/2/142)
- Bouchet, L., Strong, A. W., Porter, T. A., et al. 2011, *ApJ*, 739, 29, doi: [10.1088/0004-637X/739/1/29](https://doi.org/10.1088/0004-637X/739/1/29)
- Brinkman, H. E., den Hartogh, J. W., Doherty, C. L., Pignatari, M., & Lugaro, M. 2021, *ApJ*, 923, 47, doi: [10.3847/1538-4357/ac25ea](https://doi.org/10.3847/1538-4357/ac25ea)
- Chatzopoulos, E., & Wheeler, J. C. 2012, *ApJ*, 748, 42, doi: [10.1088/0004-637X/748/1/42](https://doi.org/10.1088/0004-637X/748/1/42)
- Chieffi, A., & Limongi, M. 2013, *ApJ*, 764, 21, doi: [10.1088/0004-637X/764/1/21](https://doi.org/10.1088/0004-637X/764/1/21)
- . 2020, *ApJ*, 890, 43, doi: [10.3847/1538-4357/ab6739](https://doi.org/10.3847/1538-4357/ab6739)
- Coc, A., Porquet, M.-G., & Nowacki, F. 1999, *Phys. Rev. C*, 61, 015801, doi: [10.1103/PhysRevC.61.015801](https://doi.org/10.1103/PhysRevC.61.015801)
- Cybur, R. H., Amthor, A. M., Ferguson, R., et al. 2010, *ApJS*, 189, 240, doi: [10.1088/0067-0049/189/1/240](https://doi.org/10.1088/0067-0049/189/1/240)
- de Angelis, A., Tatischeff, V., Grenier, I. A., et al. 2018, *Journal of High Energy Astrophysics*, 19, 1, doi: [10.1016/j.jheap.2018.07.001](https://doi.org/10.1016/j.jheap.2018.07.001)
- de Jager, C., Nieuwenhuijzen, H., & van der Hucht, K. A. 1988, *A&AS*, 72, 259
- Diehl, R., Dupraz, C., Bennett, K., et al. 1995, *A&A*, 298, 445
- Diehl, R., Lugaro, M., Heger, A., et al. 2021, *PASA*, 38, e062, doi: [10.1017/pasa.2021.48](https://doi.org/10.1017/pasa.2021.48)
- Ekström, S., Georgy, C., Eggenberger, P., et al. 2012, *A&A*, 537, A146, doi: [10.1051/0004-6361/201117751](https://doi.org/10.1051/0004-6361/201117751)
- Ertl, T., Janka, H. T., Woosley, S. E., Sukhbold, T., & Ugliano, M. 2016, *ApJ*, 818, 124, doi: [10.3847/0004-637X/818/2/124](https://doi.org/10.3847/0004-637X/818/2/124)
- Falla, A., Roberti, L., Limongi, M., & Chieffi, A. 2025, *ApJ*, 991, 21, doi: [10.3847/1538-4357/adfa05](https://doi.org/10.3847/1538-4357/adfa05)
- Farmer, R., Fields, C. E., Petermann, I., et al. 2016, *ApJS*, 227, 22, doi: [10.3847/1538-4365/227/2/22](https://doi.org/10.3847/1538-4365/227/2/22)
- Farmer, R., Laplace, E., Ma, J.-z., de Mink, S. E., & Justham, S. 2023, *ApJ*, 948, 111, doi: [10.3847/1538-4357/acc315](https://doi.org/10.3847/1538-4357/acc315)
- Feige, J., Wallner, A., Altmeyer, R., et al. 2018, *PhRvL*, 121, 221103, doi: [10.1103/PhysRevLett.121.221103](https://doi.org/10.1103/PhysRevLett.121.221103)
- Fuller, G. M., Fowler, W. A., & Newman, M. J. 1982, *ApJ*, 252, 715, doi: [10.1086/159597](https://doi.org/10.1086/159597)
- Gao, B., Giraud, S., Li, K. A., et al. 2021, *PhRvL*, 126, 152701, doi: [10.1103/PhysRevLett.126.152701](https://doi.org/10.1103/PhysRevLett.126.152701)
- Grevesse, N., & Sauval, A. J. 1998, *SSRv*, 85, 161, doi: [10.1023/A:1005161325181](https://doi.org/10.1023/A:1005161325181)
- Heger, A., Langer, N., & Woosley, S. E. 2000, *ApJ*, 528, 368, doi: [10.1086/308158](https://doi.org/10.1086/308158)
- Heger, A., & Woosley, S. E. 2010, *ApJ*, 724, 341, doi: [10.1088/0004-637X/724/1/341](https://doi.org/10.1088/0004-637X/724/1/341)
- Herwig, F. 2000, *A&A*, 360, 952, doi: [10.48550/arXiv.astro-ph/0007139](https://doi.org/10.48550/arXiv.astro-ph/0007139)
- Jermyn, A. S., Bauer, E. B., Schwab, J., et al. 2023, *ApJS*, 265, 15, doi: [10.3847/1538-4365/aca8d](https://doi.org/10.3847/1538-4365/aca8d)
- Karakas, A. I. 2010, *MNRAS*, 403, 1413, doi: [10.1111/j.1365-2966.2009.16198.x](https://doi.org/10.1111/j.1365-2966.2009.16198.x)
- Langanke, K., & Martínez-Pinedo, G. 2001, *Atomic Data and Nuclear Data Tables*, 79, 1, doi: [10.1006/adnd.2001.0865](https://doi.org/10.1006/adnd.2001.0865)
- Limongi, M., & Chieffi, A. 2006, *ApJ*, 647, 483, doi: [10.1086/505164](https://doi.org/10.1086/505164)
- . 2018, *ApJS*, 237, 13, doi: [10.3847/1538-4365/aacb24](https://doi.org/10.3847/1538-4365/aacb24)
- Lin, R. P., Dennis, B. R., Hurford, G. J., et al. 2002, *SoPh*, 210, 3, doi: [10.1023/A:1022428818870](https://doi.org/10.1023/A:1022428818870)

- Lugaro, M., & Karakas, A. I. 2008, *NewAR*, 52, 416, doi: [10.1016/j.newar.2008.05.005](https://doi.org/10.1016/j.newar.2008.05.005)
- Lugaro, M., Ott, U., & Kereszturi, Á. 2018, *Progress in Particle and Nuclear Physics*, 102, 1, doi: [10.1016/j.pnpnp.2018.05.002](https://doi.org/10.1016/j.pnpnp.2018.05.002)
- Maeder, A., & Meynet, G. 2001, *A&A*, 373, 555, doi: [10.1051/0004-6361:20010596](https://doi.org/10.1051/0004-6361:20010596)
- Mahoney, W. A., Ling, J. C., Jacobson, A. S., & Lingenfelter, R. E. 1982, *ApJ*, 262, 742, doi: [10.1086/160469](https://doi.org/10.1086/160469)
- McEnery, J., van der Horst, A., Dominguez, A., et al. 2019, in *Bulletin of the American Astronomical Society*, Vol. 51, 245, doi: [10.48550/arXiv.1907.07558](https://doi.org/10.48550/arXiv.1907.07558)
- Nugis, T., & Lamers, H. J. G. L. M. 2000, *A&A*, 360, 227
- O'Connor, E., & Ott, C. D. 2011, *ApJ*, 730, 70, doi: [10.1088/0004-637X/730/2/70](https://doi.org/10.1088/0004-637X/730/2/70)
- Ostdiek, K. M., Anderson, T. S., Bauder, W. K., et al. 2017, *Phys. Rev. C*, 95, 055809, doi: [10.1103/PhysRevC.95.055809](https://doi.org/10.1103/PhysRevC.95.055809)
- Palacios, A., Meynet, G., Vuissoz, C., et al. 2005, *A&A*, 429, 613, doi: [10.1051/0004-6361:20041757](https://doi.org/10.1051/0004-6361:20041757)
- Paxton, B., Bildsten, L., Dotter, A., et al. 2011, *ApJS*, 192, 3, doi: [10.1088/0067-0049/192/1/3](https://doi.org/10.1088/0067-0049/192/1/3)
- Paxton, B., Cantiello, M., Arras, P., et al. 2013, *ApJS*, 208, 4, doi: [10.1088/0067-0049/208/1/4](https://doi.org/10.1088/0067-0049/208/1/4)
- Paxton, B., Marchant, P., Schwab, J., et al. 2015, *ApJS*, 220, 15, doi: [10.1088/0067-0049/220/1/15](https://doi.org/10.1088/0067-0049/220/1/15)
- Paxton, B., Schwab, J., Bauer, E. B., et al. 2018, *ApJS*, 234, 34, doi: [10.3847/1538-4365/aaa5a8](https://doi.org/10.3847/1538-4365/aaa5a8)
- Pignatari, M., Hirschi, R., Wiescher, M., et al. 2013, *ApJ*, 762, 31, doi: [10.1088/0004-637X/762/1/31](https://doi.org/10.1088/0004-637X/762/1/31)
- Prantzos, N. 2004, *A&A*, 420, 1033, doi: [10.1051/0004-6361:20035766](https://doi.org/10.1051/0004-6361:20035766)
- Rugel, G., Faestermann, T., Knie, K., et al. 2009, *PhRvL*, 103, 072502, doi: [10.1103/PhysRevLett.103.072502](https://doi.org/10.1103/PhysRevLett.103.072502)
- Salpeter, E. E. 1955, *ApJ*, 121, 161, doi: [10.1086/145971](https://doi.org/10.1086/145971)
- Schneider, F. R. N., Podsiadlowski, P., & Müller, B. 2021, *A&A*, 645, A5, doi: [10.1051/0004-6361/202039219](https://doi.org/10.1051/0004-6361/202039219)
- Smith, D. M. 2004, in *ESA Special Publication*, Vol. 552, 5th INTEGRAL Workshop on the INTEGRAL Universe, ed. V. Schoenfelder, G. Lichti, & C. Winkler, 45, doi: [10.48550/arXiv.astro-ph/0404594](https://doi.org/10.48550/arXiv.astro-ph/0404594)
- Spyrou, A., Richman, D., Couture, A., et al. 2024, *Nature Communications*, 15, 9608, doi: [10.1038/s41467-024-54040-4](https://doi.org/10.1038/s41467-024-54040-4)
- Sukhbold, T., Ertl, T., Woosley, S. E., Brown, J. M., & Janka, H.-T. 2016, *ApJ*, 821, 38, doi: [10.3847/0004-637X/821/1/38](https://doi.org/10.3847/0004-637X/821/1/38)
- Sukhbold, T., & Woosley, S. E. 2014, *ApJ*, 783, 10, doi: [10.1088/0004-637X/783/1/10](https://doi.org/10.1088/0004-637X/783/1/10)
- Timmes, F. X., Woosley, S. E., Hartmann, D. H., et al. 1995, *ApJ*, 449, 204, doi: [10.1086/176046](https://doi.org/10.1086/176046)
- Tomsick, J., & COSI Collaboration. 2022, in 37th International Cosmic Ray Conference, 652, doi: [10.22323/1.395.0652](https://doi.org/10.22323/1.395.0652)
- Tur, C., Heger, A., & Austin, S. M. 2010, *ApJ*, 718, 357, doi: [10.1088/0004-637X/718/1/357](https://doi.org/10.1088/0004-637X/718/1/357)
- Vedrenne, G., Roques, J.-P., Schönfelder, V., et al. 2003, *A&A*, 411, L63, doi: [10.1051/0004-6361:20031482](https://doi.org/10.1051/0004-6361:20031482)
- Vink, J. S., de Koter, A., & Lamers, H. J. G. L. M. 2001, *A&A*, 369, 574, doi: [10.1051/0004-6361:20010127](https://doi.org/10.1051/0004-6361:20010127)
- Wallner, A., Bichler, M., Buczak, K., et al. 2015, *PhRvL*, 114, 041101, doi: [10.1103/PhysRevLett.114.041101](https://doi.org/10.1103/PhysRevLett.114.041101)
- Wang, W., Harris, M. J., Diehl, R., et al. 2007, *A&A*, 469, 1005, doi: [10.1051/0004-6361:20066982](https://doi.org/10.1051/0004-6361:20066982)
- Wang, W., Siebert, T., Dai, Z. G., et al. 2020, *ApJ*, 889, 169, doi: [10.3847/1538-4357/ab6336](https://doi.org/10.3847/1538-4357/ab6336)
- Weaver, T. A., Zimmerman, G. B., & Woosley, S. E. 1978, *ApJ*, 225, 1021, doi: [10.1086/156569](https://doi.org/10.1086/156569)
- Woosley, S. E., & Heger, A. 2007, *PhR*, 442, 269, doi: [10.1016/j.physrep.2007.02.009](https://doi.org/10.1016/j.physrep.2007.02.009)
- Woosley, S. E., Heger, A., & Weaver, T. A. 2002, *Reviews of Modern Physics*, 74, 1015, doi: [10.1103/RevModPhys.74.1015](https://doi.org/10.1103/RevModPhys.74.1015)
- Woosley, S. E., & Weaver, T. A. 1988, *PhR*, 163, 79, doi: [10.1016/0370-1573\(88\)90037-3](https://doi.org/10.1016/0370-1573(88)90037-3)
- Xin, W., Nomoto, K., & Zhao, G. 2025, arXiv e-prints, arXiv:2502.11012, doi: [10.48550/arXiv.2502.11012](https://doi.org/10.48550/arXiv.2502.11012)
- Xin, W., Nomoto, K., Zhao, G., & Wu, W. 2023, *Chinese Physics C*, 47, 034107, doi: [10.1088/1674-1137/aca1ff](https://doi.org/10.1088/1674-1137/aca1ff)